Article

Evidence from ab initio and transport modeling for diffusion-driven zirconium isotopic fractionation in igneous rocks

Xi Chen, Wenzhong Wang, Zhe Zhang, Xike Nie, and Nicolas Dauphas

Just Accepted

Evidence from *ab initio* and transport modeling for diffusion-driven zirconium isotopic fractionation in igneous rocks

Xi Chen[1*], Wenzhong Wang[2,3], Zhe Zhang[1], Xike Nie[4], Nicolas Dauphas[1]

[1]Origins Laboratory, Department of the Geophysical Sciences and Enrico Fermi Institute, The University of Chicago, Chicago, IL 60637, USA

[2]School of Earth and Space Sciences, University of Science and Technology of China, Hefei, China

[3]Department of Earth Sciences, University College London, London, UK

[4]Carnegie Institution for Science, Washington, DC 20005, USA

*To whom correspondence should be addressed (chenxicindy@uchicago.edu)

10885 words, 29 figures, 3 tables, 10 videos

August 18th, 2020

1

Abstract

23

24   We use density functional theory (DFT) to calculate the equilibrium isotopic fractionation

25   factors of zirconium (Zr) in a variety of minerals including zircon, baddeleyite, Ca-catapleiite,

26   ilmenite, geikielite, magnetite, apatite, K-feldspar, quartz, olivine, clinopyroxene, orthopyroxene,

27   amphibole, and garnet. We also report equilibrium isotopic fractionation factors for Hf in zircons,

28   Ca-catapleiite, and ilmenite. These calculations show that coordination environment is an

29   important control on Zr and Hf isotopic fractionation, with minerals with Zr and Hf in low

30   coordinations predicted to be enriched in the heavy isotopes of Zr and Hf, relative to those with Zr

31   and Hf in high coordinations. At equilibrium, zircon, which hosts Zr and Hf in 8-fold coordination,

32   is predicted to have low $^{94}Zr/^{90}Zr$ and $^{179}Hf/^{177}Hf$ ratios compared to silicate melt, which hosts

33   Zr and Hf in 6-fold coordination. However, our modeling results indicate that little equilibrium

34   isotopic fractionation for Zr is expected during magmatic differentiation and zircon crystallization.

35   We show through isotopic transport modeling that the Zr isotopic variations that were

36   documented in igneous rocks are likely due to diffusion-driven kinetic isotopic fractionation. The

37   two settings where this could take place are (*i*) diffusion-limited crystallization of zircon (DLC

38   model) and (ii) diffusion-triggered crystallization of zircon (DTC model) in the boundary layer

39   created by the growth of Zr-poor minerals. Fractional crystallization of zircons enriched in light

40   Zr isotopes by diffusion can drive residual magmas towards heavy Zr isotopic compositions. Our

41   diffusive transport model gives the framework to interpret Zr isotope data and gain new insights

42   into the cooling history of igneous rocks and the setting of zircon crystallization.

43   **Keywords:** *isotopes, equilibrium fractionation, diffusive transport, zirconium, hafnium*

1
2
3   **1. Introduction**

44

45   High Field Strength Elements [HFSEs; Ti(IV), Zr(IV), Hf(IV), Nb(V), Ta(V)] have high ionic

46   charge (Z) over radius (r) ratio. They behave incompatibly during magmatic processes, resulting

47   in their enrichment in the continental crust relative to the bulk silicate Earth (by factors of ~3 to

48   24[1,2]). They are insoluble in aqueous fluids under most circumstances, and are characterized by

49   low concentrations and short residence times in seawater (Zr: 5600 yr, Hf: 1300 yr[3], Ti: 150 yr[4]).

50   They are highly refractory, with 50% condensation temperatures under solar nebula conditions of

51   1546 to 1741 K for Zr and Hf, respectively[5,6]. Because of all these characteristics (incompatibility,

52   insolubility in aqueous fluids, and refractoriness), they have proven to be extremely useful in

53   geochemistry for normalizing concentrations of water-soluble[7,8] and moderately volatile[9] elements.

54   HFSEs are also useful in their own right: (1) In cosmochemistry, their relative abundances in

55   refractory inclusions are found to be fractionated by high-temperature evaporation/condensation

56   processes[10–15]. (2) The ^{176}Lu-^{176}Hf decay system ($t_{1/2}$= 37.8 Gyr) has been widely used as both a

57   chronometer and a tracer of planetary differentiation processes[16–19]. (3) Titanium enrichment

58   during fractional crystallization is a feature that distinguishes tholeiitic from calc-alkaline series[20]

59   (other trace HFSEs can also be used to distinguish these two series[21]). (4) The sub-chondritic

60   Nb/Ta ratios in all the major terrestrial reservoirs (the missing Nb-paradox) points to the existence

61   of high-temperature processes that can fractionate these twin elements at large scales[22–27]. (5) The

62   elevated Ti, Ta, and Nb (TITAN) concentrations in ocean island basalts with high ^{3}He/^{4}He

63   indicates the presence of a non-primitive recycled component in the deep mantle[28]. (6) The

64   abundances and isotopes of these elements in terrigenous sediments can help constrain the nature

65   (felsic or mafic) of the provenance region of the detritus[29–31].

3

66   Isotopic variations that depart from the laws of mass-dependent fractionation[32] have been

67   documented for Ti, Zr, and Hf. These variations arise from (1) incomplete mixing of

68   nucleosynthetic anomalies for Ti[33–40], Zr[41–43] and Hf[42,44–46], (2) cosmogenic neutron capture effects

69   from irradiation of solar system materials by cosmic rays for Ti[47] and Hf[48,49], and (3) radioactive

70   decay of short-lived ^{92}Nb ($t_{1/2}$= 34.7 Myr) for ^{92}Zr[50–52], and long-lived ^{176}Lu for ^{176}Hf[16,17,53,54]. Over

71   the past several years, considerable progress has been made in documenting the mass-dependent

72   component of isotopic variations for Ti[55–62] and Zr[63–69]. Mass-dependent Ti isotopic variations in

73   calcium-aluminum-rich inclusions (CAIs) reflect evaporation/condensation processes[58,59].

74   Titanium isotopic variations have also been found in igneous rocks resulting from mantle

75   depletion[56,60] and magmatic differentiation[55,57,61,62]. These variations are driven by differences in

76   coordination between Ti in melt and minerals[55,62,70]. Zirconium isotopic variations have more

77   recently been documented in igneous rocks and minerals[63–69] but the mechanism responsible for

78   those variations is uncertain.

79   Much focus in recent Zr isotope studies has focused on zircon ($ZrSiO_4$). Zircon is an accessory

80   mineral commonly found in igneous, metamorphic and detrital sedimentary rocks. It can be readily

81   dated using the U-Pb system and hosts important geochemical tracers (Hf, U, Th and REE). These

82   features, combined with the high resistance of zircon to secondary processes, have made it the

83   focus of a wide variety of geochemical, petrological, and geological studies interrogating major

84   questions of Earth sciences, such as the timing of mass extinctions, onset of subduction, and growth

85   and maturation of the continental crust[19,54,71–79].

86   Zirconium has five naturally occurring stable isotopes, ^{90}Zr (51.45%), ^{91}Zr (11.22%), ^{92}Zr

87   (17.15%), ^{94}Zr (17.38%) and ^{96}Zr (2.80%). Zirconium isotopic compositions are typically reported

88   in δ^{94}Zr or δ'^{94}Zr notations, which are departures in permil (‰) of the ^{94}Zr/^{90}Zr ratio relative to a

89   reference material. Zirconium stable isotope systematics is a relatively new field and there is no

90   widespread agreement on which reference material to use. In the following, we report $\delta^{94}Zr$ values

91   relative to NIST 3169[67]. Zirconium isotopic analyses have also been reported relative to a NIST

92   standard under development[66] and the IPGP-Zr standard[63–69]. Converting Zr isotopic compositions

93   from NIST 3169 to IPGP-Zr would involve shifting all $\delta^{94}Zr$ values by ~ -0.04 ‰[67,69].

94   The role that zircon plays in controlling Zr isotopic fractionation in igneous rocks is debated.

95   Inglis et al.[64] measured the Zr isotopic compositions of bulk magmatic rocks from Hekla volcano

96   and found that $\delta^{94}Zr$ increases with SiO_2 content, which is a tracer of magmatic differentiation.

97   Combining these data with the zirconium concentrations of these rocks, they concluded that zircon

98   crystallization within the Hekla differentiation suite was the main driver of the observed variations

99   in the bulk samples. They argued based on coordination considerations that equilibrium isotopic

100   fractionation could explain qualitatively why zircon would preferentially incorporate light Zr

101   isotopes, leaving the residual melt enriched in heavy Zr isotopes (elevated $\delta^{94}Zr$ values). Feng et

102   al.[67] and Tian et al.[69] found that among igneous rock standards, felsic rocks tend to have heavier

103   Zr isotopic compositions than mafic rocks, which agree with the trend documented by Inglis et

104   al.[63,64]. Ibanez-Mejia and Tissot[66] measured single zircon and baddeleyite crystals from an

105   anorthositic gabbro (FC-1) and found widespread $\delta^{94}Zr$ values ranging from -4.3 to +0.9 ‰. Unlike

106   Inglis et al.[64], they argued that their data could be explained using a distillation model if zircon and

107   baddeleyite were isotopically heavy relative to the melt from which they crystallized, driving the

108   residual liquid to extremely low $\delta^{94}Zr$ values. The rocks measured in these studies were different

109   and the discrepancy illustrates the fact that the driver behind Zr isotopic fractionation in igneous

110   rocks remains highly uncertain, which limits the usefulness of this system to draw petrogenetic

111   inferences on zircon formation based on Zr isotopic analyses. Zhang et al.[65] analyzed the Zr

5

112   isotopic compositions in several zircons using laser ablation multiple collector inductively coupled

113   plasma mass spectrometry (LA-MC-ICPMS) and found relatively constant values.

114   Available Zr isotopic data[63–69] in igneous rocks hint at the possibility that they could provide

115   new insights into the conditions of zircon formation but there are outstanding questions that need

116   to be addressed before Zr isotopes can be developed into a useful petrogenetic tracer. Are the

117   measured variations the result of equilibrium fractionation between minerals and melts? If yes, is

118   it the crystallization of zircon or other Zr-bearing phases that drives Zr isotopic fractionation

119   measured in bulk rocks? Alternatively, are the observed variations due to kinetic processes such

120   as diffusion? If yes, what does it tell us about magma cooling and zircon crystallization history?

121   Hafnium has very similar chemical behavior to zirconium. It possesses six stable or long-

122   lived (the half live of ^{174}Hf is $\sim 2\times 10^{15}$ yr) isotopes ^{174}Hf (0.16%), ^{176}Hf (5.26%), ^{177}Hf (18.60%),

123   ^{178}Hf (27.28%), ^{179}Hf (13.62%) and ^{180}Hf (35.08%). To our knowledge, no high precision

124   measurements of Hf stable isotopic fractionation have been reported. As discussed in the present

125   manuscript, such data would shed light on the processes responsible for Zr isotopic fractionation

126   in igneous rocks.

127   To understand what controls Zr isotopic variations in igneous rocks, we have performed *ab*

128   *initio* calculations of the equilibrium isotopic fractionation factors of Zr and Hf in a variety of

129   minerals using the technique of density functional theory (DFT). Following Farges et al.[80], Ca-

130   catapleiite ($CaZrSi_3O_9 \cdot 2H_2O$) was used as a model structure for Zr in silicate melts. The Zr-rich

131   minerals investigated here are zircon ($ZrSiO_4$) and baddeleyite (ZrO_2). We also investigated

132   equilibrium isotopic fractionation for Zr in a variety of minerals where Zr substitutes other

133   elements: ilmenite ($FeTiO_3$), geikielite ($MgTiO_3$), apatite ($Ca_5(PO_4)_3F$), magnetite ($MgFe_2O_4$),

134   forsterite (Mg_2SiO_4), diopside ($MgCaSi_2O_6$), enstatite ($MgSiO_3$), K-feldspar ($KAlSi_3O_8$), quartz

6

135 (SiO_2), tremolite ($Ca_2Mg_5Si_8O_{22}(OH)_2$) and pyrope ($Mg_3Al_2(SiO_4)_3$). Besides these calculations,

136 we have also explored how diffusion-driven kinetic isotopic fractionation during crystallization of

137 zircon and other Zr-poor minerals could fractionate Zr isotopes in igneous rocks. We find that both

138 (1) diffusion-limited zircon crystallization from a supersaturated liquid and (2) Zr diffusion in the

139 liquid boundary-layer around a Zr-poor growing crystal, can explain the Zr isotopic variations that

140 have been documented in igneous rocks. Our favored scenario is that the Zr isotopic variations

141 documented in some zircons reflect their crystallizations in a supersaturated diffusion boundary

142 layer, in a process of diffusion-triggered crystallization.

143

144 **2. Methods**

145 **2.1. Equilibrium mass-dependent isotopic fractionation**

146   Equilibrium mass-dependent isotopic fractionation arises from changes in vibrational

147 frequencies caused by isotopic substitution of an element in a given system[81,82]. Following

148 Bigeleisen and Goeppert-Mayer[81], the reduced partition function ratio β_A of an element X in Phase

149 A, which represents the isotope fractionation factor between Phase A and an ideal gas of X atoms,

150 can be expressed within the quasi-harmonic approximation as,

$$\beta_A = \frac{Q_h}{Q_l} = \prod_i^{3N} \frac{u_{ih}}{u_{il}} \frac{e^{-\frac{1}{2}u_{ih}}}{1-e^{-u_{ih}}} \frac{1-e^{-u_{il}}}{e^{-\frac{1}{2}u_{il}}} \ . \tag{1}$$

152 where h and l represent the heavy and light isotopes respectively, i is a running index of vibrational

153 frequency mode, N is the number of atoms in the unit cell, and Q_h and Q_l refer to the vibrational

154 partition function for the heavy and light isotopes, respectively. A phase with N atoms has *3N*

155 vibrational modes and thus the product runs over all *3N* phonon modes. u_{ih} and u_{il} are defined as,

$$u_i = \hbar\omega_i/k_BT \ . \tag{2}$$

157 where $\hbar$ and k_B is the reduced Planck constant and Boltzmann constant, respectively, T is

7

158   temperature in Kelvin, and ω_i is the vibrational frequency of the ith mode. Equilibrium isotopic

159   fractionation between two phases A and B in the δ-notation is readily calculated from the reduced

160   partition function ratio using the following formula,

$$\Delta_{A-B} \simeq 10^3 ln\alpha_{A-B} = 10^3 ln\beta_A - 10^3 ln\beta_B. \tag{3}$$

162   For a given phase, $10^3 ln\beta$ can be expressed as a polynomial expansion of even powers of the

163   inverse of the temperature[83,84],

$$10^3 ln\beta = \frac{A_1}{T^2} + \frac{A_2}{T^4} + \frac{A_3}{T^6}. \tag{4}$$

165   where the coefficients A_1, A_2, and A_3 can be calculated from the even moments of the phonon

166   density of states[84]. The first term in this equation is proportional to the mean force constant $\langle F \rangle$ (in

167   N/m) of the chemical bonds that the element of interest forms with the coordination atoms,

$$A_1 = 1000 \left(\frac{1}{m_l} - \frac{1}{m_h} \right) \frac{\hbar^2}{8k_B^2} \langle F \rangle. \tag{5}$$

169   At the high temperatures relevant to igneous system, this term is the dominant control on

170   equilibrium isotopic fractionation[84–86]. For the $^{94}Zr/^{90}Zr$ and $^{179}Hf/^{177}Hf$ ratios, we have,

$$1000 ln\beta(^{94}Zr/^{90}Zr) \simeq 2081\langle F \rangle/T^2. \tag{6}$$

$$1000 ln\beta(^{179}Hf/^{177}Hf) \simeq 278\langle F \rangle/T^2. \tag{7}$$

173   We follow Dauphas et al.[84,87] and use the mean force constant $\langle F \rangle$ to discuss equilibrium

174   isotopic fractionation factors. The virtues of this approach for non-traditional stable isotopes are:

175   (1) It is a number that is usually easy to remember when reported in SI unit (the same units

176   as a spring constant), typically spanning the range 0 to ~1000 N/m.

177   (2) It does not depend on the choice of isotopes used to define isotopic fractionation, so one

178   can compare values from different publications regardless of the choice that are made in reporting

179   isotopic fractionation.

180   (3) It allows easy comparison of isotopic fractionation between different elements. For

181   example, when comparing Zr and Hf equilibrium isotope fractionations, the difference could result

182   from a difference in the masses of the isotopes of the two elements, and/or from a difference in the

183   nature of the bonds (force constant).

184   (4) Bond strength is the governing factor for equilibrium isotopic fractionation, especially at

185   high temperature. We use Eq. 4 to calculate equilibrium fractionation factors at all temperatures

186   and recommend that this equation be used in future studies, but the truncated Eqs. 5 to 7 are

187   adequate above ~300 °C.

188   For the reasons outlined above, we have used the mean force constant $\langle F \rangle$ in a number of

189   publications discussing equilibrium isotopic fractionation[84,87–91] and we encourage the community

190   to use this quantity more broadly in non-traditional stable isotope geochemistry.

191

2.2. First-principle calculations

193   We performed first-principle calculations based on density functional theory (DFT) using

194   VASP (Vienna Ab Initio Simulation Package) with the projector-augmented wave (PAW)

195   method[92]. The generalized-gradient approximation (GGA)[93] for the exchange-correlation

196   functional was adopted and the PAW-PBE pseudopotentials were used. The energy cutoff for all

197   calculations was 600 eV. All mineral structures, including cell parameters and atomic positions,

198   were well relaxed at ambient pressure. The Brillouin zone summations over the electronic states

199   were performed at different k-point grids according to their unit cell sizes (**Table S1**). For all

200   structure optimizations, the residual forces converge within 10^{-3} eV/Å. In order to estimate the β

201   factors of ^{94}Zr/^{90}Zr for all phases, we performed full calculations of phonon vibration frequencies

202   using the finite displacement method as implemented in the open-source code PHONOPY[94].

203

2.3. Mineral structures

205 The DFT approach is better suited to calculate the equilibrium isotopic fractionation for

206 periodic crystals or small molecules. DFT can in principle tackle liquids but it is computationally

207 challenging to run such calculations[90,95–98], and while there are good constraints to ground truth

208 calculations involving ions in water, the structure of silicate melts remains poorly known. For those

209 reasons, we have decided to use knowledge from X-ray Absorption Fine Structure (EXAFS)

210 spectroscopy on the local structure of Zr in silicate melts to select a model crystal composition to

211 simulate Zr dissolved in silicate liquid. Farges et al.[80] found that regardless of the glass investigated,

212 Zr^{4+} at a trace level of $\sim$2000 ppm in silicate glass was mainly in 6-coordinated sites and had a

213 local structural environment similar to that in the mineral catapleiite (with a similar Zr-O bond

214 length of $\sim$2.07-2.10 Å)[80], a 3-tetrahedra zirconium cyclosilicate (the synthetic sodium zirconium

215 cyclosilicate Lokelma is used to treat hyperkalemia in patients[99,100]). The atomic positions of H

216 atoms in catapleiite ($Na_2ZrSi_3O_9 \cdot 2H_2O$) have not been reported, and cannot be properly modeled

217 by DFT. We have therefore selected the similar Ca-catapleiite ($CaZrSi_3O_9 \cdot 2H_2O$) in which all

218 atomic positions are well known, to use as the model structure for Zr in silicate melt.

219 The calculated minerals in this study include zircon, baddeleyite, Ca-catapleiite, geikielite,

220 ilmenite, magnetite, apatite, K-feldspar, quartz, olivine, clinopyroxene, orthopyroxene, amphibole

221 and garnet. Zirconium is a trace element in these minerals except for zircon, baddeleyite, and Ca-

222 catapleiite.

223 In spinel-facies lherzolite and harzburgite, the inventories of Zr and Hf are dominated by

224 clinopyroxene and to a lesser extent orthopyroxene[101]. In garnet lherzolite, the inventories of Zr

225 and Hf are dominated by garnet and clinopyroxene, with again orthopyroxene playing a lesser

226   role[102]. Although major element sites in these minerals are well known, the substitution

227   mechanisms for Zr incorporation as a minor element remain unclear. In olivine, clinopyroxene,

228   and orthopyroxene, there are two possible Zr substitution mechanisms. One is that Zr^{4+} directly

229   occupies the tetrahedral Si site ($^{IV}Si^{4+} \leftrightarrow Zr^{4+}$), and the other one is that Zr substitutes in the

230   octahedral Mg site or the dodecahedral Ca site (in clinopyroxene) with charge balanced by nearby

231   Mg vacancies ($^{VI}Mg^{2+}/^{VIII}Ca^{2+} + {}^{VI}Mg^{2+} \leftrightarrow Zr^{4+}_{Mg/Ca} + \square$).

232   Olivine has one equivalent tetrahedral Si site and two nonequivalent octahedral Mg sites (M1

233   and M2) with M2 site being larger than M1 site. For the substitution $^{IV}Si^{4+} \leftrightarrow Zr^{4+}$, we constructed

234   a Zr-doped olivine by replacing one Si atom with one Zr atom in a supercell of forsterite. For the

235   substitution $^{VI}Mg^{2+} + {}^{VI}Mg^{2+} \leftrightarrow Zr^{4+} + \square$, the nearest neighbor $[^{VI}Mg^{2+}]$-$[^{VI}Mg^{2+}]$ pair is replaced by

236   Zr^{4+} and a vacancy ($\square$). There are four different possible configurations for this substitution:

237      $[^{VI}Mg^{2+}]_{M1}$-$[^{VI}Mg^{2+}]_{M1}$, $[^{VI}Mg^{2+}]_{M1}$-$[^{VI}Mg^{2+}]_{M2}$, $[^{VI}Mg^{2+}]_{M2}$-$[^{VI}Mg^{2+}]_{M1}$,   and $[^{VI}Mg^{2+}]_{M2}$-

238      $[^{VI}Mg^{2+}]_{M2}$, where we substitute the first $^{VI}Mg^{2+}$ of each pair by Zr^{4+} and the second is replaced by

239   a vacancy. Our calculations show that the Zr-doped olivine with Zr^{4+} occupying the M2 Mg site

240   and the charge balanced by the nearest M1 Mg vacancy ($[^{VI}Mg^{2+}]_{M2}$-$[^{VI}Mg^{2+}]_{M1}$) has the lowest

241   total energy among all nonequivalent configurations. This configuration with the lowest energy

242   was used for the calculation.

243   Orthopyroxene also has two nonequivalent Mg sites (M1 and M2) and two nonequivalent Si

244   sites (SiA and SiB). Our calculations show that the energy difference between Zr^{4+} in the SiA and

245   SiB sites is large, 7.6 eV for $Mg_{32}Si_{31}ZrO_{96}$ orthopyroxene, suggesting that Zr^{4+} prefers the SiB

246   site. Thus, orthopyroxene with Zr^{4+} occupying the SiB site was used for the substitution

247      $^{IV}Si^{4+} \leftrightarrow Zr^{4+}$. Similar to the substitution $^{VI}Mg^{2+} + {}^{VI}Mg^{2+} \leftrightarrow Zr^{4+} + \square$ in olivine, we also considered

248   four configurations for the $Zr^{4+} + \square$ substitution: $[^{VI}Mg^{2+}]_{M1}$-$[^{VI}Mg^{2+}]_{M1}$, $[^{VI}Mg^{2+}]_{M1}$-$[^{VI}Mg^{2+}]_{M2}$,

249    $[^{VI}Mg^{2+}]_{M2}$-$[^{VI}Mg^{2+}]_{M1}$, and $[^{VI}Mg^{2+}]_{M2}$-$[^{VI}Mg^{2+}]_{M2}$. The Zr-doped orthopyroxene, in which Zr^{4+}

250   occupies the M1 Mg site with the charge balanced by the nearest M2 Mg vacancy ($[^{VI}Mg^{2+}]_{M1}$-

251    $[^{VI}Mg^{2+}]_{M2} \leftrightarrow Zr^{4+} + $) has the lowest total energy and was used in the calculations.

252   Diopside, the $CaMgSi_2O_6$ end-member of clinopyroxene, contains four equivalent Ca atoms,

253   four equivalent Mg atoms, and eight equivalent Si atoms. A Zr-doped clinopyroxene with the

254   substitution $^{IV}Si^{4+} \leftrightarrow Zr^{4+}$ can be produced by replacing one Si atom with one Zr atom. We also

255   investigated the Zr-doped clinopyroxene with the substitution $^{VIII}Ca^{2+}/^{VI}Mg^{2+}+$

256    $^{VI}Mg^{2+} \leftrightarrow Zr^{4+}_{Ca/Mg} + $, in which $Zr^{4+}+$ can substitute for any pair $[^{VIII}Ca^{2+}]$-$[^{VI}Mg^{2+}]$, $[^{VII}Mg^{2+}]$-

257    $[^{VIII}Ca^{2+}]$, or $[^{VI}Mg^{2+}]$-$[^{VI}Mg^{2+}]$. Our calculations show that the Zr-doped diopside with Zr^{4+}

258   occupying the Mg site and the charge balanced by a vacancy in the nearest Ca site ($[^{VII}Mg^{2+}]$-

259    $[^{VIII}Ca^{2+}] \leftrightarrow Zr^{4+} + $) has a lower total energy than the configuration with $[^{VIII}Ca^{2+}]$-

260    $[^{VI}Mg^{2+}] \leftrightarrow Zr^{4+} + $ (*i.e.*, -2.3 eV for $Ca_7Mg_7ZrSi_{16}O_{48}$), indicating that Zr^{4+} preferentially enters

261   the Mg site in diopside. This is consistent with the experimental finding that Zr is located in the

262   M1 (Mg) site in clinopyroxene[103].

263   Tremolite has three nonequivalent Mg sites (M1, M2, and M3) and two nonequivalent Si sites

264   (SiT1 and SiT2). The volume of Mg-O octahedron increases in the order of M3 < M1 < M2. For

265   the substitution $^{IV}Si^{4+} \leftrightarrow Zr^{4+}$, the configuration with Zr^{4+} occupying the larger SiT2 site has a lower

266   energy and was used for the calculation. For the substitution $^{VI}Mg^{2+} + {}^{VI}Mg^{2+} \leftrightarrow Zr^{4+} + $, tremolite

267   has six different $[^{VI}Mg^{2+}]$-$[^{VI}Mg^{2+}]$ pairs: $[^{VI}Mg^{2+}]_{M1}$-$[^{VI}Mg^{2+}]_{M1}$ (3.17 Å), $[^{VI}Mg^{2+}]_{M2}$-$[^{VI}Mg^{2+}]_{M2}$

268   (5.59 Å), $[^{VI}Mg^{2+}]_{M3}$-$[^{VI}Mg^{2+}]_{M3}$ (10.27 Å), $[^{VI}Mg^{2+}]_{M1}$-$[^{VI}Mg^{2+}]_{M2}$ (3.08 Å), $[^{VI}Mg^{2+}]_{M1}$-

269    $[^{VI}Mg^{2+}]_{M3}$ (3.08 Å), and $[^{VI}Mg^{2+}]_{M2}$-$[^{VI}Mg^{2+}]_{M3}$ (3.18 Å). Here we only consider $[^{VI}Mg^{2+}]$-

270    $[^{VI}Mg^{2+}]$ pairs where the two Mg sites are in close proximity, corresponding to seven different

271   configurations ($[^{VI}Mg^{2+}]_{M1}$-$[^{VI}Mg^{2+}]_{M1}$, $[^{VI}Mg^{2+}]_{M1}$-$[^{VI}Mg^{2+}]_{M2}$, $[^{VI}Mg^{2+}]_{M2}$-$[^{VI}Mg^{2+}]_{M1}$,

12

272 $[^{VI}Mg^{2+}]_{M1}$-$[^{VI}Mg^{2+}]_{M3}$, $[^{VI}Mg^{2+}]_{M3}$-$[^{VI}Mg^{2+}]_{M1}$, $[^{VI}Mg^{2+}]_{M2}$-$[^{VI}Mg^{2+}]_{M3}$, and $[^{VI}Mg^{2+}]_{M3}$-

273 $[^{VI}Mg^{2+}]_{M2}$) that could be replaced by Zr^{4+} . Our calculations show that the structure with Zr^{4+}

274 occupying the largest M2 Mg site with the charge balanced by the nearest M1 Mg vacancy

275 ($[^{VI}Mg^{2+}]_{M2}$-$[^{VI}Mg^{2+}]_{M1}$↔Zr^{4+}) has the lowest energy and was therefore used in the calculations.

276 This choice is consistent with spectroscopic evidence indicating that in arfvedsonite (a sodium

277 amphibole mineral), Zr is in the M2 site[103].

278   The initial structure of Zr-doped quartz was constructed through the substitution $^{IV}Si^{4+}$↔Zr^{4+},

279 while the Zr-doped structure for K-feldspar was constructed by substituting Zr^{4+} for K^+/Al^{3+} with

280 the charge balanced by a tetrahedral Al^{3+}/K^+ vacancy ($^{VIII}K^+$+ $^{IV}Al^{3+}$↔Zr^{4+}_{K+} and

281 $^{IV}Al^{3+}$+$^{VIII}K^+$↔Zr^{4+}_{Al+}). Our calculations show that the configuration with

282 $^{IV}Al^{3+}$+$^{VIII}K^+$↔Zr^{4+}_{Al+} has a lower energy than $^{VIII}K^+$+ $^{IV}Al^{3+}$↔Zr^{4+}_{K+} (*i.e.*, -4.7 eV for

283 $K_7Al_7ZrSi_{24}O_{64}$). The former was therefore used in the calculations.

284   Previous work suggested that Zr could substitute for Ca in apatite[104], we generated the initial

285 structure of Zr-doped apatite by substituting one Zr atom for one nine-coordinated Ca atom, with

286 the charge balanced by the vacancy in the nearest seven-coordinated Ca site ($^{IX}Ca^{2+}$+

287 $^{VII}Ca^{2+}$↔Zr^{4+}_{IX-Ca+}).

288   For geikielite ($MgTiO_3$) and ilmenite ($FeTiO_3$), the Zr-doped structures were generated by

289 the substitution $^{VI}Ti^{4+}$↔Zr^{4+} due to the similarity between Ti^{4+} and Zr^{4+}. For $MgFe_2O_4$ magnetite,

290 Zr^{4+} occupies the octahedral Fe^{3+} site with charge balanced by the nearest tetrahedral Fe^{3+} replaced

291 by Mg^{2+} ($^{VI}Fe^{3+}$+ $^{IV}Fe^{3+}$↔Zr^{4+}_{VI-Fe}+ Mg^{2+}_{IV-Fe}).

292   Pyrope, the Mg endmember of garnet, contains 160 atoms in its conventional cell with space

293 group Ia-3d. Here we consider three possible substitution mechanisms: (1) $^{IV}Si^{4+}$↔Zr^{4+}, where

294 Zr^{4+} occupies the tetrahedral Si site, (2) $^{VI}Al^{3+}$+ $^{IV}Si^{4+}$↔Zr^{4+}+ Al^{3+}, where Zr^{4+} occupies the

13

295   octahedral Al site and the original Al^{3+} occupies the nearest Si site, and (3) $^{VIII}Mg^{2+}+$

296    $^{VIII}Mg^{2+}\leftrightarrow Zr^{4+}+$, where Zr^{4+} occupies the dodecahedral Mg site with the charge balanced by

297   replacement of the nearest Mg site with a vacancy. Spectroscopic data seems to support the

298   presence of Zr in 6-fold coordination in garnet[103], which would be support of the second

299   substitution mechanism $^{VI}Al^{3+}+{}^{IV}Si^{4+}\leftrightarrow Zr^{4+}+Al^{3+}$.

300   Zirconium are present as trace element in many of these minerals. We modelled various levels

301   of Zr dilution in olivine, orthopyroxene, clinopyroxene, tremolite, quartz, geikielite, ilmenite,

302   apatite, K-feldspar, and magnetite by incorporating Zr into their supercells, which were generated

303   by expanding the primitive cell along different directions. For example, the 112-atom and 224-

304   atom supercells of olivine were obtained by expanding the primitive cell twice along the *a* and *c*

305   directions and twice simultaneously along *a*, *b*, and *c* directions, respectively. Substituting one Si

306   atom with one Zr atom in those supercells can produce olivine structures with Zr/(Zr+Si) of 1/16

307   and 1/32, respectively. The same approach was used to simulate dilution in other minerals (**Table**

308   **1**).

309   For the calculations of Hf equilibrium isotopic fractionation, we investigated Ca-catapleiite

310   and zircon (Hf substituting Zr) as well as ilmenite (Hf substituting Ti). For zircon and Ca-

311   catapleiite, we calculated the mineral structures and β-factors for different Zr/Hf ratios using a

312   supercell approach (**Table 1**).

313   The relaxed cell parameters and volumes of zircon, baddeleyite, and Ca-catapleiite are

314   compared with experimental measurements at 300 K in **Table S2**. Our calculations with GGA

315   overestimate the volumes of these minerals by ~3-4%, which is typical of GGA calculations, as

316   already noticed in previous studies[105–108]. In general, the local density approximation (LDA) tends

317   to underestimate the volume, while GGA tends to give a larger volume than experimental data.

14

318   DFT calculations will also give different β factors when different exchange-correlation functionals

319   are used. However, the differences in $10^3 \ln\beta$ (*i.e.*, $10^3 \ln\alpha$ or equilibrium isotope fractionation

320   factors between minerals), are less sensitive to the approximation adopted for the change-

321   correlation functional[105–108]. We compare the calculated frequencies of zircon and baddeleyite with

322   experimental data in **Fig. S1**. Our results agree with experimental measurements, with a

323   slope between calculated and measured frequencies of 0.966±0.04. Following the uncertainty

324   analysis presented by Meheut *et al.*[109], we estimate that the uncertainties of our calculated $\ln\beta$ and

325    $\ln\alpha$ values at high temperature are ~6 and 8% relative, respectively.

326

3. Results

328   The average Zr-O bond lengths and Zr coordination numbers (CNs) in all calculated minerals

329   are listed in **Table 1**. The average Zr-O bond length and Zr CN depend on the threshold adopted

330   for Zr-O bond lengths. In all calculated minerals, the Zr-O distances form two populations, ranging

331   from 1.9 Å to 2.4 Å, or greater than 3.0 Å. Here we adopted a value of 2.4 Å as the cutoff to

332   determine Zr-O bond lengths and Zr CNs. The Zr CN ranges from 4 in silicate minerals with the

333   substitution $Si^{4+} \leftrightarrow Zr^{4+}$ to 8 in zircon, and the average Zr-O bond length ranges from 1.960 Å in

334   olivine with the substitution $Si^{4+} \leftrightarrow Zr^{4+}$ to 2.228 Å in zircon. In addition, within the explored

335   compositional space (**Table 1**), there is no significant Zr concentration effect on the average Zr-O

336   bond lengths in Zr-doped minerals.

337   As discussed in Section 2.1. and references therein, the main control on equilibrium isotopic

338   fractionation is the bond strength or force constant, and at high temperature $1000\ln\beta$ is directly

339   proportional to $\langle F \rangle$. The Zr force constants vary from 280 to 566 N/m in the calculated minerals

340   (**Table 1**). In all minerals, Zr is primarily coordinated with oxygen and as expected[110], the main

15

341   control on the bond strength (force constant) is coordination (**Fig. 1A**), which is also manifested

342   as a correlation between force constant with bond length (**Fig. 1B**). The average Zr force constants

343   of minerals in 4, 6, 7, and 8 coordination are 540, 366, 323, 340 N/m respectively. Among them,

344   ilmenite (6-fold coordination), magnetite (6), apatite (6), baddeleyite (7) and zircon (8) have

345   weaker Zr-O bonds than that of 6-fold coordination Ca-catapleiite, the silicate melt proxy mineral.

346   Geikielite (6-fold coordination) and most of the silicate minerals with Zr in mostly 4- and 6-fold

347   coordination have stronger Zr-O bonds than that of 6-fold coordinated Ca-catapleiite. Pyrope with

348   the substitution $^{VIII}Mg^{2+} + ^{VIII}Mg^{2+} \leftrightarrow Zr^{4+} +$ is the only silicate mineral calculated with a weaker

349   Zr-O bond strength than the melt.

350   The $1000\ln\beta$ values of $^{94}Zr/^{90}Zr$ of all calculated minerals can be expressed as a function of

351   temperature ($10^3\ln\beta = A_1x + A_2x^2 + A_3x^3$, where $x = 10^6/T^2$ and T is temperature in Kelvin; Eq. 4). The

352   coefficients of this polynomial expansion are listed in **Table 1**. For many non-traditional stable

353   isotopes systems, one can relate equilibrium fractionation at any temperature to an expansion in

354   the even powers of $\langle F \rangle^{87,111}$. For a Debye phonon density of states (PDOS), we would have,

$$1000\ln\beta \simeq 1000\left(\frac{m_h}{m_l} - 1\right)\left(\frac{\gamma}{8}\frac{\langle F \rangle}{T^2} - \frac{5\gamma^2}{2016}\frac{\langle F \rangle^2}{T^4} + \frac{25\gamma^3}{326592}\frac{\langle F \rangle^3}{T^6}\right). \qquad (8)$$

356   with $\gamma = \hbar^2/(k_B^2 m_h)$. Phonon density of states of naturally occurring minerals rarely follow a

357   Debye profile and we can improve on this formula by writing a more general, semi-empirical

358   equation,

$$1000\ln\beta \simeq B_1\langle F \rangle/T^2 - B_2\langle F \rangle^2/T^4 + B_3\langle F \rangle^3/T^6. \qquad (9)$$

360   with $B_1 = 1000(1/m_l - 1/m_h)\,\hbar^2/(8k_B^2)$, and B_2 and B_3 constants that depend on the element

361   and isotopes considered (and to some extent the particular PDOS, although these are second order

362   corrections and the exact shape of the PDOS does not matter too much). We have calculated the

363   values of B_2 and B_3 by regressing A_2 *vs.* $\langle F \rangle^2$ and A_3 *vs.* $\langle F \rangle^3$ (**Figs. S2, S3**) for the purpose of

16

364   evaluating the validity of the high-temperature approximation. Note that the equivalent regressions

365   of A_2 *vs.* $A_1{}^2$ and A_3 *vs.* $A_1{}^3$ provide a rapid means of assessing the consistency of the polynomial

366   expansion as an erroneous reporting of the coefficients would show up as an outlier in these

367   diagrams. We find the approximate formula,

$$1000\ln\beta(^{94}Zr/^{90}Zr) \simeq 2081\langle F\rangle/T^2 - 2.5 \times 10^4\langle F\rangle^2/T^4 + 8.5 \times 10^5\langle F\rangle^3/T^6. \quad (10)$$

369   In **Fig. 2A** (also see **Fig. S4**), we use this formula to calculate the extent to which the high-

370   temperature approximation (truncating the polynomial to the first order; Eq. 6, 9, and 10) can

371   approximate the true value of $1000\ln\beta$ (Eq. 4) as a function of T and $\langle F\rangle$ (see Fig. 3 of Dauphas

372   et al.[84] for a similar figure for iron). As shown, given that the force constants of Zr bonds in all

373   calculated minerals are between 280 and 566 N/m, we find that provided that the temperature is

374   higher than ~300-500 °C, truncating the expansion to the first order gives a $1000\ln\beta$ value that is

375   within 1% of the value given by the whole expansion. For most high-temperature applications in

376   metamorphic and igneous geochemistry and petrology, the high-temperature approximation

377    $1000\ln\beta \simeq 2081\langle F\rangle/T^2$ is therefore valid.

378   The Zr-doped silicate minerals with the substitution $Si^{4+}\leftrightarrow Zr^4$ have significantly larger β

379   factors than other species. This is mainly because Zr in these silicate minerals form stiffer bonds

380   due to the incorporation of Zr into the low-coordination (IV) tetrahedral Si site. At 1000 K, the

381    $1000\ln\beta$ values range from 1.17 ‰ in Zr-doped olivine (substituting Si) to 0.58 ‰ in Zr-doped

382   ilmenite (substituting Ti). It decreases in the order of Zr-doped olivine (substituting Si), quartz,

383   orthopyroxene, K-feldspar (substituting Al) ~ tremolite (substituting Si) ~ clinopyroxene

384   (substituting Si) ~ pyrope (substituting Si) > pyrope (substituting Al) > geikielite (substituting Ti)

385   ~ orthopyroxene, clinopyroxene, tremolite, and olivine (substituting Mg) > Ca-catapleiite > pyrope

386   (substituting Mg) > zircon ~ baddeleyite > apatite (substituting Ca) ~ $MgFe_2O_4$ magnetite

17

387   (substituting Fe) > ilmenite (substituting Ti). The temperature dependence of the reduced partition

388   function ratio ($1000\ln\beta$), as well as the equilibrium fractionation factors between minerals and

389   melt ($1000ln\alpha_{mineral-melt}$; taking Ca-catapleiite as a silicate melt proxy) are shown in **Fig. 3**. As

390   expected, they scale linearly with $1/T^2$.

391   We have also performed some *ab initio* calculations substituting Hf for Zr in several minerals

392   showing a wide range of Zr bond strengths: zircon, Ca-catapleiite, and ilmenite (**Fig. 4**). The force

393   constants of Hf bonds are very similar to those of Zr (**Table 1** and **Fig. 5**), defining a linear

394   correlation,

$$\langle F_{\mathrm{Hf}} \rangle = (1.032 \pm 0.021)\langle F_{\mathrm{Zr}} \rangle . \tag{11}$$

396   By regressing A_2 *vs.* $\langle F \rangle^2$ and A_3 *vs.* $\langle F \rangle^3$ (**Fig. S3**), we derive a one-parameter approximate

397   equation for the $1000\ln\beta$ value of Hf,

$$1000\ln\beta(^{179}\mathrm{Hf}/^{177}\mathrm{Hf}) \simeq 278\langle F \rangle/T^2 - 3464\langle F \rangle^2/T^4 + 175551\langle F \rangle^3/T^6 . \tag{12}$$

399   As with Zr (**Fig. 2A**; also see **Fig. S4**) and Fe[84], we use this formula to calculate the extent to which

400   truncating the formula to the first term $1000\ln\beta(^{179}\mathrm{Hf}/^{177}\mathrm{Hf}) \simeq 278\langle F \rangle/T^2$ (Eq. 7) provides an

401   adequate approximation of the $1000\ln\beta$ value (Eq. 4; **Fig. 2B** and **Fig. S5**). We find that provided

402   that the temperature is higher than ~300-500 °C, truncating the expansion to the first order gives a

403   $1000\ln\beta$ value that is within 1% of the value given by the whole expansion. As with Zr, the first

404   term of the polynomial gives an adequate description of equilibrium Hf isotopic fractionation for

405   applications in igneous and metamorphic geochemistry/petrology.

406   Given the near-identical force constants of Zr and Hf, the ratio of equilibrium fractionation

407   factors is directly related to the mass of the isotopes involved through (combine Eqs. 6 and 7),

$$\frac{1000\ln\alpha(^{94}\mathrm{Zr}/^{90}\mathrm{Zr})}{1000\ln\alpha(^{179}\mathrm{Hf}/^{177}\mathrm{Hf})} = \frac{2081}{278} = 7.5 . \tag{13}$$

409

18

410 **4. Discussion**

411   As we mentioned in the introduction, the use of Zr isotopic fractionation as a petrogenetic

412 tracer of zircon formation is hampered by our lack of understanding of what controls this

413 fractionation.

414   Zirconium isotopic analyses reported thus far on bulk rocks and individual zircons[63–69] yield

415 contradictory evidence with regard to what controls the observed Zr isotopic variations, and

416 whether zircons are enriched in the light or heavy isotopes of Zr relative to coexisting magma.

417 Below we use the newly established fractionation factors to show that equilibrium zircon-melt

418 fractionation cannot account for the large Zr isotopic variations that have been documented. These

419 fractionations are most likely explained by diffusion-driven kinetic isotopic fractionation.

420

421 **4.1. Equilibrium Zr isotopic fractionation during zircon crystallization from silicate melts**

422   Zircon is an important carrier of Zr and Hf in igneous rocks, so we start by focusing on the

423 effects of the equilibrium crystallization of this mineral on the behavior of Zr and Hf stable isotopes

424 during magmatic differentiation. Following Inglis et al.[64] and Ibanez-Meija and Tissot[66], we model

425 Zr isotopic fractionation during zircon crystallization using a Rayleigh distillation model,

$$426 \qquad \delta'^{94}Zr_{melt} = \delta'^{94}Zr_0 + \Delta_{Zr}^{zircon\text{-}melt} \ln f_{Zr} \,. \qquad (14)$$

427 where $\delta'^{94}Zr_{melt}$ and $\delta'^{94}Zr_0$ are the Zr isotopic compositions of the residual and starting melt

428 respectively, expressed as $\delta'^{94}Zr = 10^3 \ln\left[(^{94}Zr/^{90}Zr)_{sample}/(^{94}Zr/^{90}Zr)_{std}\right]$, f_{Zr} is the fraction

429 of Zr remaining in the melt, and $\Delta_{Zr}^{zircon\text{-}melt} = 1000\ln\alpha_{Zr}^{zircon\text{-}melt}$ is the instantaneous isotopic

430 fractionation factor of Zr between zircon and melt. The Zr isotopic composition of the

431 instantaneous zircon crystallized from the melt can be calculated as,

$$432 \qquad \delta'^{94}Zr_{i,zircon} = \delta'^{94}Zr_0 + \Delta_{Zr}^{zircon\text{-}melt}(1+\ln f_{Zr}) \,. \qquad (15)$$

19

433 The zirconium isotopic composition of the cumulative zircon is obtained by mass-balance with the

434 residual melt and initial composition,

$$\delta'^{94}\text{Zr}_{c,\text{zircon}} = \delta'^{94}\text{Zr}_0 - \Delta_{\text{Zr}}^{\text{zircon-melt}} \frac{f_{\text{Zr}}}{1-f_{\text{Zr}}} \ln f_{\text{Zr}} \;. \tag{16}$$

436 Both Inglis et al.[64] and Ibanez-Meija and Tissot[66] derived apparent $\Delta_{\text{Zr}}^{\text{zircon-melt}}$ values from

437 their measurements. The $\Delta_{\text{Zr}}^{\text{zircon-melt}}$ values that they calculated have opposite directions and

438 different magnitudes. Inglis et al.[64] found that Zr in the melt becomes isotopically heavy in the

439 course of magmatic differentiation of the Hekla volcano, meaning that zircon must be enriched in

440 the light Zr isotopes. They were able to fit their data with an instantaneous fractionation

441 $\Delta_{\text{Zr}}^{\text{zircon-melt}} = -0.5$ ‰. Ibanez-Meija and Tissot[66] measured many zircons from an anorthositic

442 gabbro (FC-1) and found that the statistical distribution of these $\delta'^{94}\text{Zr}$ values extended to very

443 negative values, which they argue is more readily explained if zircon crystallizing from the melt

444 was enriched in the heavy isotopes of Zr, and the most negative $\delta'^{94}\text{Zr}$ values resulted from

445 crystallization from a melt that has experienced extensive distillation. By fitting their statistical

446 distribution, they obtain $\Delta_{\text{Zr}}^{\text{zircon-melt}} = +1.06$ ‰. These two studies focused on different materials

447 (bulk rocks sampling a magmatic differentiation trend in the case of Inglis et al.[64]; individual

448 zircons sampling fractional crystallization within a single rock in the case of Ibanez-Meija and

449 Tissot[66]). Based on available data, it is impossible to tell what is the cause of the discrepancy

450 between these two studies and whether the measurements reflect equilibrium or diffusion-driven

451 kinetic isotopic fractionation, as has been demonstrated previously for Mg and Fe in igneous

452 rocks[112–116].

453 We have calculated Zr force constants of 335 and 369 N/m for zircon and Ca-catapleiite (the

454 silicate melt proxy), respectively (Table 1). The slightly higher force constant of Ca-catapleiite

455   relative to zircon is consistent with its lower coordination number (6 for catapleiite *vs.* 8 for zircon).

456   The equilibrium Zr isotopic fractionation between zircon and melt is given by the formula,

457    $$\Delta^{94}Zr_{\text{zircon-melt}}^{\text{eq}} = -\frac{7.87\times10^4}{T^2} + \frac{1.94\times10^9}{T^4} - \frac{5.85\times10^{13}}{T^6}. \qquad (17)$$

458   At the temperatures relevant to igneous zircon crystallization of ~700-1000 °C, the

459   equilibrium fractionation would only be -0.048 to -0.081 ‰ (**Fig. 6**). The lower $\delta'^{94}Zr$ value of

460   zircon relative to silicate melt at equilibrium is due to differences in coordination numbers. The

461   equilibrium fractionation is opposite in sign to the inferred instantaneous zircon-melt fractionation

462   of Ibanez-Meija and Tissot[66] and is much smaller in magnitude than the values given by both Inglis

463   et al.[64] and Ibanez-Meija and Tissot[66]. Taken at face value, this would suggest that the

464   instantaneous Zr isotopic fractionations measured in these two studies do not reflect equilibrium.

465   A caveat to this comparison is that we used Zr in 6-fold coordination in Ca-catapleiite ($\langle F \rangle = 369$

466   N/m) as a proxy for Zr in silicate melt. As shown in **Table 1** and **Fig. 1A**, Zr in 6-fold coordination

467   in other minerals has force constants that range between 280 and 433 N/m. Using these values for

468   Zr in melt and 335 N/m for zircon would result in zircon-melt equilibrium fractionations in the

469   range -0.12 to +0.21 ‰ above 700 °C. These values are again much smaller than the values inferred

470   by Inglis et al.[64] and Ibanez-Meija and Tissot[66], strengthening the case that the values given in

471   these two studies do not reflect zircon-melt equilibrium.

472   We further evaluate below how combining Zr isotopic compositions with Zr/Hf ratios can

473   help identify zircons that grew in equilibrium with the melt. By equilibrium, we mean that zircon

474   growth increments were in equilibrium with the bulk melt but distillation effects can still be present

475   if Zr self-diffusion was too slow for the zircon interior to equilibrate with its rim, or if zircons were

476   sequestered from the melt. The degree of isotopic fractionation in the instantaneous fraction of

477   zircon crystallizing in equilibrium with the melt is given by (combining Eqs. 15 and 17),

21

478
$$\delta'^{94}Zr_{i,zircon} = \delta'^{94}Zr_0 - \frac{7.87 \times 10^4}{T^2}(1 + \ln f_{Zr}). \tag{18}$$

479 In **Fig. 7**, we plot the value of $\delta'^{94}Zr_{i,zircon}$ for different Zr fractions in zircon $(1 - f_{Zr})$ and two

480 temperatures of 700 and 1000 °C. As shown, at equilibrium the slightly lower $\delta'^{94}Zr$ value of

481 zircon relative to the melt can drive the melt to evolve toward heavy $\delta'^{94}Zr$ values, reaching +0.25 ‰

482 (at 700 °C) and +0.14 ‰ (at 1000 °C) at 95% crystallization. One way to assess whether the data

483 can be explained by equilibrium is to combine $\delta'^{94}Zr$ with Zr/Hf analyses. Indeed, these two

484 observables should correlate in a predictable manner during equilibrium zircon crystallization as

485 they both depend on T and f_{Zr}. Zircon is a solid solution of zircon ($ZrSiO_4$) and hafnon ($HfSiO_4$),

486 and Hf zoning is often observed due to zircon growth while the melt composition evolves by

487 fractional crystallization. Zirconium is more compatible than Hf in zircon, resulting in a decrease

488 of the Zr/Hf ratio during fractional crystallization of zircon. Such Zr/Hf fractionations have been

489 documented within zircon grains (from core to margin) and in bulk rocks[117–119]. Similar to $\delta'^{94}Zr$,

490 we can model Zr/Hf fractionation using a Rayleigh distillation equation:

491
$$(Zr/Hf)_{melt} = (Zr/Hf)_0 \, f_{Zr}^{1-1/K_d}. \tag{19}$$

492 where $(Zr/Hf)_{melt}$ is the ratio in the melt, $(Zr/Hf)_0$ is the initial melt ratio, f_{Zr} is the fraction of

493 the remaining Zr in melt, and K_d is the Zr/Hf exchange coefficient between zircon and melt,

494
$$\frac{(Zr/Hf)_{zircon,inst}}{(Zr/Hf)_{melt}} = K_d. \tag{20}$$

495 We thus have,

496
$$(Zr/Hf)_{zircon,inst} = K_d \, (Zr/Hf)_0 \, f_{Zr}^{1-1/K_d}. \tag{21}$$

497 The zircon Zr/Hf ratio is not only a function of the extent of fractional crystallization but also a

498 function of temperature. Aranovich and Bortnikov[120] proposed the following formula for K_d,

499
$$K_d = e^{1531/T - 0.883}. \tag{22}$$

22

500   In **Fig. 8**, we plot the calculated trends of Zr/Hf and δ'^{94}Zr variations in growth increments

501   of zircon crystallized from silicate melt. The free parameters are the fraction of Zr remaining in

502   melt (f_{Zr} from 0.99 to 0.01) and the crystallization temperature, which we keep fixed for simplicity

503   (T from 870 to 600 °C; calculations are done using equations 15 and 17, 21 and 22). We use an

504   initial Zr/Hf ratio of 31.1, initial δ'^{94}Zr value of -0.086 ‰ [66], and the equilibrium isotopic

505   fractionation factor inferred here $\Delta^{94}\text{Zr}^{eq}_{\text{zircon-melt}} = -\frac{7.87 \times 10^4}{T^2}$ (Eq. 17). We also plot the current

506   analytical uncertainties of Zr/Hf ratio ($\pm 1\%$) and δ'^{94}Zr isotopic composition ($\pm 0.01‰$). The

507   δ'^{94}Zr value is mostly sensitive to the extent of crystallization, while Zr/Hf ratio depends on both

508   temperature and extent of crystallization. By plotting Zr/Hf and δ'^{94}Zr values in zircons, ideally

509   measured along depth profiles[65,68], one will be able to compare the results with theoretical

510   predictions, test whether zircon grew in increments in equilibrium with coexisting melt, and assess

511   the temperature (T) and extent (f_{Zr}) of zircon crystallization.

512

513   **4.2. Equilibrium Zr isotopic fractionation before the onset of zircon crystallization in melts**

514   Within the magmatic temperature range of zircon crystallization, our *ab initio* calculation

515   results show limited equilibrium isotopic fractionation between zircon and melt (see **Fig. 6**). This

516   can explain the homogenous Zr isotope compositions of those reference zircons reported in Zhang

517   et al.[65] and Tompkins et al.[68], but it fails to explain the observations made at the Hekla volcano[64]

518   and zircons and baddeleyites from the FC-1 anorthositic gabbro[66]. This implies that the current

519   observed δ'^{94}Zr variations cannot be simply explained by the mechanism of equilibrium mass-

520   dependent Zr isotopic fractionation between zircon and melt.

521   Below, we investigate whether equilibrium crystallization of other phases could have

522   controlled Zr isotopic fractionation during magmatic differentiation. We used the Rhyolite-

23

523   MELTS program[121] to calculate the evolution of Zr concentration and isotopic composition during

524   magmatic differentiation before the onset of zircon crystallization. The melt major-element

525   compositions and temperature at each step in the Rhyolite-MELTS run were used as input in the

526   zircon saturation models of Waston and Harrison[122] and Boehnke et al.[123] to check if zircon was

527   saturated, as we were primarily interested here in evaluating the influence of the crystallization of

528   non-zircon phases on the isotopic composition of Zr during magmatic differentiation (see **Fig. S6**).

529   Two starting melt compositions were used to represent calc-alkaline and tholeiitic magmatic

530   series[55,124]. Both crystallization processes start at the calculated liquidus temperatures and at 1 kbar

531   for calc-alkaline and 0.6 kbar for tholeiitic magma, respectively. For every 5℃ temperature

532   decrease, the major element compositions and mass of melt and crystallizing minerals are

533   calculated using Rhyolite-MELTS. At each step the program gives the proportions of every

534   mineral crystallizing. As a trace element, Zr is not incorporated in Rhyolite-MELTS program, but

535   its distribution among the phases can be calculated based on partition data (**Fig. 9**). The Zr partition

536   coefficients ($K_{mineral/melt}$) of each mineral in different rock matrix were compiled from the

537   GERM database. The compiled values vary in a wide range, due in part to the dependence of

538   partition coefficients on melt composition and temperature. We use the geometric mean of the

539   partition coefficients as fiducial values, and also consider the maxima and minima to assess

540   uncertainties associated with partition data. Knowing the mass fractions of minerals that crystallize,

541   the Zr partition coefficients between bulk rock and melts are calculated at each step, and mass

542   balance between melt and bulk crystallizing solids is then used to calculate the Zr concentration in

543   melt at each step. We also track the evolution of the Zr/Hf ratio and Hf concentration, using

544   literature data for the Zr/Hf exchange coefficients between minerals and melt.

545   Expectedly, Zr and Hf concentrations in the melt increase during fractional crystallization

546   before zircon saturation (**Fig. 10**). In calc-alkaline magmas, about 16% of the total zirconium and

547   10% of the total hafnium are removed by crystallizing solids before zircon saturation. In tholeiitic

548   magmas, about 13% of total zirconium and 10% of total hafnium are removed (**Figs. S7** and **S8**).

549   These removal fractions $(1 - f_{Zr}; 1 - f_{Hf})$ depend on the values of the partition coefficients that

550   are used and they range from 6 to 47% for Zr, and 3 to 32% for Hf in calc-alkaline magma (**Fig.**

551   **S7**), and from 4 to 60% for Zr and 2 to 52% for Hf in tholeiitic magma (**Fig. S8**). In **Fig. 10**, we

552   compare the modeling results for Zr and Hf concentrations with compilations of igneous rock

553   compositions from the Andes and Iceland (compiled from GEOROC database, see also Fig. S1 in

554   Ptacek et al.[31]), which typically follow calc-alkaline and tholeiitic magma series, respectively (**Fig.**

555   **10**). The expected different trends of [Zr] *vs*. SiO_2 (or [Hf] *vs*. SiO_2) between calc-alkaline and

556   tholeiitic series can be explained by the earlier crystallization of SiO_2-rich plagioclase in tholeiitic

557   series compared with calc-alkaline series melts[125–128]. Overall, all partition data (minimum,

558   geometric mean, and maximum) reproduce well the trends seen in natural calc-alkaline Andes

559   samples, while only the maximum partition data reproduce the tholeiitic Iceland samples. The bulk

560   solid-liquid Zr partition coefficient values are mainly affected by clinopyroxene and feldspar (**Fig.**

561   **9**).

562   With the same mass-balance rationale, we model the Zr isotopic evolution trends using the

563   fractionation factors between minerals and melt from our *ab initio* calculation results. Although

564   feldspar and clinopyroxene have the most leverage on Zr concentration, we find that iron-titanium

565   oxides (ilmenite and magnetite) have the potential to produce non-negligible mass-dependent

566   fractionation of Zr isotopes before the onset of zircon crystallization (see **Fig. 3B**). The modeling

567   trends in **Fig. 11** show that both for calc-alkaline and tholeiitic magma, the $\delta'^{94}Zr$ value of the

25

568   melt evolves towards light values before zircon starts to crystallize (**Fig. 11**). The magnitudes of

569   the isotopic fractionations are small, ranging from −0.005 to −0.160 ‰ for tholeiitic series and

570   from −0.016 to −0.165 ‰ for calc-alkaline series. These values are conservative estimates

571   because we considered all possible substitution mechanisms (see **Table 1**) and the fractionations

572   would have been smaller if we had solely used the substitution favored by spectroscopic

573   observations for clinopyroxene[103]. Our modeling results thus show that before the onset of zircon

574   crystallization, magmatic differentiation is not expected to impart large Zr isotopic fractionation

575   in the magma if equilibrium prevails.

576

4.3. Diffusion-driven kinetic isotopic fractionations during crystal growth from silicate melt

578   The discussions in the previous two sections show that magmatic differentiation processes

579   are unlikely to be associated with significant equilibrium Zr isotopic fractionation. This suggests

580   that the large Zr isotopic fractionations measured in bulk volcanic rocks[64] and igneous zircons and

581   baddeleyites[66] are more likely the product of kinetic isotope effects.

582   While equilibrium isotopic fractionation decreases rapidly with increasing temperature,

583   kinetic effects associated with diffusion can remain significant at magmatic temperature[129]. Such

584   diffusive fractionations have been documented in natural magmatic systems for Mg and Fe in

585   olivine[112–116] and Mg in melts[130]. Such non-equilibrium variations in natural systems can result

586   from diffusion-limited transport in both melts[131–133] and crystals[112–116]. In the case of zircon,

587   Ibanez-Mejia and Tissot[66] pointed out that Zr diffusivity in zircon is extremely slow. If any kinetic

588   isotopic fractionation is present in zircon and other non-zircon minerals, it is most likely due to

589   diffusion in the melt[131–133].

26

590   We examine below two models of kinetic fractionation of Zr isotopes resulting from diffusion

591   in melts (**Fig. 12**) that can explain the Zr isotopic variations that have been documented in igneous

592   rocks: (i) diffusion-limited growth of zircon in a supersaturated magma and (ii) diffusion in the

593   boundary layer formed during the growth of a Zr-poor mineral. Several studies have examined

594   diffusive isotopic fractionation during crystal growth. Jambon[131] presented the first model of

595   isotopic fractionation of major and trace elements in magmas associated with crystal growth. They

596   assumed a constant growth rate ($dr/dt = v$, with v constant) and examined a planar geometry.

597   Watson and Muller[132] also assumed a constant growth rate, but examined a spherical geometry and

598   allowed for advective transport outside of a boundary layer. Dauphas and Rouxel[133] presented

599   analytical equations for diffusion-limited concretion/crystal growth for both planar and spherical

600   geometries. The main difference with Jambon[131] and Watson and Muller[132] is that the growth rate

601   of the crystal is assumed to be limited by diffusion and therefore varies with time ($dr/dt \propto 1/\sqrt{t}$).

602   DePaolo[134] examined Ca and Mg isotopic fractionation during carbonate formation.

603   The reason why isotopes can be fractionated by diffusion in magmatic systems is that light

604   (L) isotopes tend to diffuse faster than the heavy ones (H), which is often parameterized as[129,135–

605   139],

$$\frac{D_H}{D_L} = \left(\frac{m_L}{m_H}\right)^{\beta}. \tag{23}$$

607   where D and m stand for diffusivity and mass of the isotopes, and β is an empirical factor. No data

608   is available documenting Zr or Hf isotopic fractionation during diffusion in silicate melts. However,

609   Watkins et al.[140] recognized that β exponents correlate with the ratio of the diffusivities of the

610   cations normalized by those of Si. The D_{Zr}/D_{Si} and D_{Hf}/D_{Si} ratios in rhyolite melts most relevant

611   to zircon crystallization are close to ~1[141]. Using the relationship established by Watkins et al.[140],

612   we calculate $\beta \simeq 0.054 \pm 0.059$ for both Zr and Hf (**Fig. 13**). Using Eq. 23, we therefore have,

27

613
$$\frac{D_{94_{Zr}}}{D_{90_{Zr}}} = \left(\frac{89.905}{93.906}\right)^{0.054\pm0.059} = 0.9977 \pm 0.0026 \quad . \qquad (24)$$

614
$$\frac{D_{179_{Hf}}}{D_{177_{Hf}}} = \left(\frac{176.943}{178.946}\right)^{0.054\pm0.059} = 0.9994 \pm 0.0007 \quad . \qquad (25)$$

615   The differences in diffusivities $D_{94_{Zr}}/D_{90_{Zr}}$ and $D_{179_{Hf}}/D_{177_{Hf}}$ are thus -2.3±2.6 and -0.6±0.7 ‰

616   (Δ_D, see Eq. A10), respectively.

617

618   **4.3.1. Diffusion-limited crystallization (DLC) of zircon**

619   The first setting where Zr isotopes could have been fractionated is during diffusion-limited

620   growth of zircon from a supersaturated medium. The growth of zircon will deplete the surrounding

621   medium in Zr, which has to be supplied by diffusion from the far-field medium[142,143]. Because

622   light isotopes diffuse faster than heavy ones, Zr delivered to the growing crystal will be enriched

623   in the light isotopes of Zr, while the medium further away will be enriched in the heavy isotopes

624   of Zr[129]. The formalism developed by Dauphas and Rouxel[133] can be applied here to model isotopic

625   fractionation during diffusion-limited growth of zircon from an infinite medium. The growth rate

626   cannot be arbitrarily set to a constant value, as it depends on the supply of Zr to the growing crystal

627   through diffusion. This has important consequences for isotopic fractionation. Most importantly,

628   during diffusion-limited growth, the δ'^{94}Zr value of the growing crystal will be offset from that of

629   the surrounding medium even when the system has reached a pseudo steady-state. The reason is

630   that the diffusive boundary layer keeps growing as the square-root of time, so from a mass-balance

631   point of view, the light isotopic enrichment of the growing crystal can be offset by the heavy

632   isotopic enrichment of the diffusive boundary layer.

633   We used the equations provided by Dauphas and Rouxel[133] to calculate the Zr concentration

634   and isotopic composition profiles in the liquid away from the interface of a spherical zircon

28

635   growing in a diffusion-limited regime and these are plotted in **Fig. 14** (we also provide movies as

636   Supporting Information **SI (E)** showing the evolutions of these two variables as a function of time,

637   **Mov. 1 and 2**, movie titles and captions are in Supporting Information **SI (D)**). Very rapidly, the

638   system reaches a pseudo steady-state whereby the concentration and isotopic profiles follow a self-

639   similar solution that stretches as the square-root of time. Dauphas and Rouxel[133] derived an

640   approximate solution for the isotopic composition of the crystal (assuming spherical geometry)

641   that is valid up to a supersaturation of $S \simeq 5$ to 10,

642
$$\delta'^{94}Zr_{\text{zircon}} \simeq \left[\frac{\Delta'^{94}Zr_{\text{eq, zircon-melt}}}{S} + \left(1 - \frac{1}{S}\right)\left(\frac{D_{94Zr}}{D_{90Zr}} - 1\right)10^3 \right]. \tag{26}$$

643   where $S = C_\infty / C_{sat}$ is the degree of supersaturation (C_∞ and C_{sat} are the far-field and saturation

644   concentrations, respectively) and $\Delta'^{94}Zr_{\text{eq, zircon-melt}}$ is the equilibrium isotopic fractionation

645   between zircon and silicate melt. Note that diffusive fractionation associated with growth of a

646   planar crystal is a factor of ~2 lower than that predicted for a sphere (Eq. 54 of Dauphas and

647   Rouxel[133]).

648   In **Fig. 15**, we plot the expected isotopic fractionation as a function of the degree of

649   supersaturation. The $\delta'^{94}Zr_{\text{zircon}}$ here is the isotopic composition in the crystal relative to that in

650   the far-field growth medium. With $\beta_{Zr} = 0.113$ in Eq. 24, we can reach a $\delta'^{94}Zr$ value for zircon

651   of -4.4 ‰. This is similar to the lowest $\delta'^{94}Zr$ values of -4.278 ‰ measured by Ibanez-Meija and

652   Tissot[66]. Ibanez-Meija and Tissot[66] found a range of $\delta'^{94}Zr$ values extending to +0.905 ‰. The

653   formula of Dauphas and Rouxel[133] assumes growth from an infinite medium. In practice, in a finite

654   system[143], the diffusive enrichment in the light isotopes of the growing crystal will leave behind a

655   residual melt that will become enriched in the heavy isotopes of Zr, so we do expect the production

656   of zircon with positive $\delta'^{94}Zr$ values. As indicated by Eq. 26, the parameter that determines

657   whether equilibrium or diffusive kinetic isotopic composition is expressed in a crystal is the degree

29

658   of supersaturation of the medium, which also influences the growth rate. Therefore, δ'^{94}Zr

659   measurements of zircons could provide direct clues on the cooling and crystallization history of

660   the host magma body. For purely diffusion-limited growth, the degree of supersaturation S

661   influences the crystal growth rate through (derived from Eq. 56 of Dauphas and Rouxel[133]; C_{zircon}

662   is the Zr concentration in zircon),

$$R = \sqrt{\frac{2C_{sat}(S-1)Dt}{C_{zircon}}} \quad . \tag{27}$$

663

$$\frac{dR}{dt} = \frac{1}{2}\sqrt{\frac{2C_{sat}(S-1)D}{C_{zircon}}}\frac{1}{\sqrt{t}} = \frac{C_{sat}(S-1)D}{RC_{zircon}} \quad . \tag{28}$$

664

$$S = 1 + \frac{dR}{dt} \times \frac{RC_{zircon}}{DC_{sat}} \quad . \tag{29}$$

665

666   Neglecting equilibrium isotopic fractionation in Eq. 26 and injecting Eq. 29 in Eq. 26, we thus

667   have,

$$\delta'^{94}\mathrm{Zr}_{\mathrm{zircon}} \simeq \left[1 - \frac{1}{1 + \frac{dR}{dt} \times \frac{RC_{zircon}}{DC_{sat}}}\right]\left(\frac{D_{94Zr}}{D_{90Zr}} - 1\right)10^3 \quad . \tag{30}$$

668

669   In **Fig. 16**, we use this equation to plot the expected Zr isotopic fractionation in zircon

670   δ'^{94}Zr$_{\mathrm{zircon}}$ as a function of growth rate dR/dt at different temperatures (different D and C_{sat}

671   values) and different supersaturations. In Eq. 30, we consider crystals of 10, 100 µm in radius (R).

672   As discussed by Zhang and Xu[142], zircons larger than ~10 µm in an open magma are expected to

673   partially grow through advection of Zr to a diffusive boundary layer. Watson and Muller[132]

674   investigated numerically the isotopic consequences of such a model. The zircons measured by

675   Ibanez-Meija and Tissot[66] are less than 10 µm in size and grew in inter-cumulus liquid pockets,

676   where advection is most likely limited. In such settings (late crystallization of residual liquid

677   pockets), it is conceivable that diffusive growth could play a role even for zircons larger than 10

678   µm. The Zr diffusivities at different temperatures are calculated using the experimental results

30

679 from Zhang and Xu[142]. Zirconium saturation concentrations (C_{sat}) at different temperatures are

680 calculated using the model presented in Boehnke et al.[123]. The Zr concentration in zircon is

681 ~500,000 ppm. The result of our calculation (**Fig. 16**) shows that the extremely light $\delta'^{94}Zr$ values

682 (-4.278 ‰) reported by Ibanez-Meija and Tissot[66] in ~10 μm zircons crystallized at ~850 °C can

683 be explained if they grew in a diffusion-limited regime at a supersaturation of ~7.8, corresponding

684 to a growth rate of ~0.4 μm/yr. We are not aware of any independent constraint on the zircon

685 growth rate in the specific anorthositic gabbro studied by Ibanez-Meija and Tissot[66], but our

686 inferred growth rate is in line with the results of Zhang and Xu[142] who gave values in the range

687 0.01-1.0 μm/yr for variably hydrated rhyolitic melts. We conclude that diffusion-limited

688 crystallization of zircon is a possible mechanism to explain the variable Zr isotopic compositions

689 measured in zircon grains[66].

690 Inglis et al.[64] argued that the heavy Zr isotopic compositions of differentiated rocks from

691 Hekla could be explained by fractional crystallization of zircon with $\delta'^{94}Zr$ values shifted by -0.5 ‰

692 relative to the melt. As shown in **Fig. 15**, such low $\delta'^{94}Zr$ values in zircon can be produced in the

693 DLC model by growth from a melt characterized by Zr supersaturations of ~1.1 to 2.2, depending

694 on the value of β_{Zr}. Zircons from the Hekla volcano are typically 40×160 μm in size and were

695 formed at temperatures of ~750-850 °C[144]. Assuming a characteristic size of 36 μm (a sphere of

696 36 μm radius has the same volume as a cylinder of 20 μm radius and 160 μm length) and a

697 temperature of 800 °C, the supersaturations of 1.1 to 2.2 correspond to growth rates of 0.0004 to

698 0.0044 μm/yr, which is slightly smaller than the range given by Zhang and Xu[142]. A caveat to this

699 calculation is that it assumes that Zr transport is entirely diffusive. Zircons would grow faster if

700 advective transport took place, which would also dampen kinetic isotopic fractionation. The

701 zircon-melt isotopic fractionation calculated by Inglis et al.[64] is uncertain as it relies solely on bulk

31

702 rock measurements. Without further isotopic characterizations of the mineral carriers of Zr in

703 Hekla, it is difficult to robustly interpret bulk rock Zr isotopic analyses. To summarize, the removal

704 of isotopically light zircon formed by the DLC process could possibly drive residual magmas to

705 evolve towards heavy Zr isotopic compositions, as is observed[64,67,69].

706

4.3.2. Diffusion-triggered crystallization (DTC) of zircon during the growth of Zr-poor

707

708 **minerals**

709   The highly fractionated zircons measured by Ibanez-Meija and Tissot[66] are closely associated

710 with plagioclase, clinopyroxene and ilmenite, and are interpreted to have crystallized from inter-

711 cumulus liquid pockets. The second setting where diffusive isotopic fractionation could have taken

712 place is therefore in the diffusive boundary layers formed around Zr-poor minerals, as was first

713 described for apatite by Harrison and Watson[145]. When Zr-poor minerals grow, Zr excluded from

714 their crystal lattice accumulates in the liquid at the interface with the solid[146], and the concentration

715 gradient thus formed relaxes by Zr diffusion from the solid-liquid interface to the far field. Because

716 light isotopes diffuse faster than heavy ones[129], Zr at the interface get enriched in the heavy

717 isotopes while the liquid further away gets enriched in the light isotopes. Zircon crystallized from

718 liquid in this boundary layer could inherit the isotopic fractionation imparted by diffusion. Given

719 the great incompatibility of Zr in most minerals, the concentration in the liquid at the interface of

720 those growing crystals could be much higher than the far-field. In steady-state and planar geometry,

721 the constant growth rate model of Smith et al.[146] predicts that the liquid at the interface can be

722 enriched relative to the far-field by a factor of $1/K$, where K is the mineral/liquid partition

723 coefficient[146]. Based on partitioning data for olivine, pyroxene, and feldspar (GERM database,

724 https://earthref.org/KDD/e:40/), we calculate that the Zr enrichments at the liquid/solid interface

32

725　could reach factors of ~7-100, ~1-70, and ~2-1100, respectively. These dramatic enrichments

726　could have led Zr concentration to exceed zircon saturation and trigger their crystallization. The

727　zircon thus formed would inherit Zr from the diffusion boundary layer, which would have been

728　fractionated isotopically by diffusive transport. We call this second model diffusion-triggered

729　crystallization (DTC) (**Fig. 12**). Note that DTC and DLC could have occurred concurrently if the

730　diffusive layer around Zr-poor minerals was highly supersaturated and the growth of zircon itself

731　was diffusion-limited.

732　　　The models of Smith et al.[146], Jambon[131] and Watson and Muller[132] are well suited to explore

733　diffusive isotopic fractionation created by the exclusion of Zr from growing Zr-poor crystals.

734　Using the framework of Smith et al.[146] for diffusive transport away from a planar crystal growing

735　at constant speed, we derive the analytical equations of the isotopic composition in the liquid and

736　solid in transient and at steady-state (see **SI (A)** for details). For the concentration, Smith et al.[146]

737　give the transient liquid concentration C_l relative to the initial (and far-field) concentration C_0 as a

738　function of (1) the distance x_l from the original interface expressed with the dimensionless

739　variable $u = \dot{R}x_l/D$, where $\dot{R} = dR/dt$ is the growth rate and D is the diffusivity in the melt, and

740　(2) the time t elapsed since the start of crystal growth expressed with the dimensionless variable

741　$w = \dot{R}^2 t/D$,

742　$\dfrac{C_l(u,w)}{C_0} = 1 + \dfrac{1-K}{2K}e^{-u}\mathrm{erfc}\left(\dfrac{u-w}{2\sqrt{w}}\right) - \dfrac{1}{2}\mathrm{erfc}\left(\dfrac{u+w}{2\sqrt{w}}\right) + \left(1 - \dfrac{1}{2K}\right)e^{-(1-K)(u+Kw)}\mathrm{erfc}\left[\dfrac{u+(2K-1)w}{2\sqrt{w}}\right].$　(31)

743　In **SI (A)**, we show that the isotopic composition in the melt can be written as,

744　$$\delta_{l,2/1} \simeq A\Delta_D + B\Delta_K \,. \tag{32}$$

745　with $\Delta_D = (D_2/D_1 - 1)1000$ the term describing isotopic fractionation imparted by differences

746　in the diffusivities of the isotopes involved, and $\Delta_K = (K_2/K_1 - 1)1000 = (\alpha_{2/1} - 1)1000$ the

747 equilibrium isotopic fractionation between mineral and melt. A and B are given by the following

748 formulas,

749
$$A = \frac{e^{-Kw - \frac{(u+w)^2}{4w}}(-1+K)\left\{2e^{u+Kw}K\sqrt{w} + e^{\frac{(u+w)^2}{4w}}\sqrt{\pi}\left[-e^{Kw}u\times\mathrm{erfc}\left(\frac{u-w}{2\sqrt{w}}\right) - e^{K(u+Kw)}(-1+2K)(u+Kw)\mathrm{erfc}\left(\frac{u+(2K-1)w}{2\sqrt{w}}\right)\right]\right\}}{\left\{\sqrt{\pi}\left[e^{u}K + e^{u}K\times\mathrm{erfc}\left(\frac{u+w}{2\sqrt{w}}\right) - (-1+K)\mathrm{erfc}\left(\frac{u-w}{2\sqrt{w}}\right) + e^{K(u+(-1+K)w)}(-1+2K)\mathrm{erfc}\left(\frac{u+(2K-1)w}{2\sqrt{w}}\right)\right]\right\}}.$$ (33)

750
$$B = \frac{e^{-\frac{(u+w)^2}{4w}}\left\{2e^{u}K(-1+2K)w + \sqrt{\pi}\sqrt{w}\left[e^{\frac{(u+w)^2}{4w}}\mathrm{erfc}\left(\frac{u-w}{2\sqrt{w}}\right) - e^{\frac{1}{4}\left((2+4K)u + \frac{u^2}{w} + (1-2K)^2 w\right)}(1 + K(-1+2K)(u+(-1+2K)w))\mathrm{erfc}\left(\frac{u+(2K-1)w}{2\sqrt{w}}\right)\right]\right\}}{\left\{\sqrt{\pi}\sqrt{w}\left[(-1+K)\mathrm{erfc}\left(\frac{u-w}{2\sqrt{w}}\right) + e^{u}K\left(-2+\mathrm{erfc}\left(\frac{u+w}{2\sqrt{w}}\right)\right) - e^{K(u+(-1+K)w)}(-1+2K)\mathrm{erfc}\left(\frac{u+(2K-1)w}{2\sqrt{w}}\right)\right]\right\}}.$$ (34)

751 In **Fig. 17**, we plot the Zr concentration and isotopic composition in the growing Zr-poor

752 crystal and melt growth medium at three times until the crystal grows to 1 cm in size (we also

753 provide movies as Supporting Information, **Mov. 3, 4 and 5**). The concentrations and isotopic

754 compositions in **Fig. 17** are normalized to those in the far-field growth medium composition. In

755 the liquid, incompatible Zr accumulates. The concentration in the solid is always in equilibrium

756 with the liquid at the interface where the two concentrations relate with each other by the partition

757 coefficient $C_{s,\text{interface}} = KC_{l,\text{interface}}$. The concentration in the growing crystal $C_{s,\text{interface}}$

758 therefore increases as the concentration in the liquid at the interface $C_{l,\text{interface}}$ builds up until the

759 concentration in the crystal is equal to that in the far-field and the liquid interface concentration is

760 enriched by a factor of $1/K$ (**Figs. 17A, 18A**). The Zr that accumulates in the liquid at the interface

761 diffuses away from that interface into the far field. Since light Zr isotopes can diffuse faster than

762 heavy ones[129], the solid-liquid interface has high δ'^{94}Zr, which is transferred into the Zr-poor

763 crystal as it grows. The liquid further away in the diffusive boundary layer has low δ'^{94}Zr (**Fig.**

764 **17B, C**). As the system evolves towards steady-state (**Fig. 18**; movies are provided as Supporting

765 Information, **Mov. 6, 7 and 8**), the isotopic composition of the crystal and the liquid interface

766 approach that of the far field medium but the liquid in the diffusive boundary layer keeps a low

767   δ'^{94}Zr value. From a mass-balance point of view, this low δ'^{94}Zr value is balanced by the high

768   δ'^{94}Zr value of the early crystal grown during the transient period.

769   As discussed above and by Harrison and Watson[145] for apatite, the elevated Zr concentration

770   in the diffusive boundary layer could trigger the saturation and crystallization of zircon (DTC

771   model). These newly-crystallized zircons would inherit some of the fractionated Zr isotopic

772   composition of the diffusive boundary layer from which they grew, which span slightly positive

773   and highly negative δ'^{94}Zr values (**Fig. 18B, C**). The most negative δ'^{94}Zr value achieved at

774   steady state is (see derivations in **SI (A)**),

$$\delta_l = 1000 \left(\frac{D_{94_{Zr}}}{D_{90_{Zr}}} - 1 \right) \times ProductLog[\frac{1-K}{eK}] \, . \tag{35}$$

776   For clinopyroxene or plagioclase, the values of K are 0.08 and 0.004 (geometric mean values for

777   equilibrium with basaltic melt, GERM database), and we would predict isotopic fractionations that

778   could reach -2.8 and -7.6 ‰, respectively for $\beta_{Zr} = 0.054$ (Eq. 24; **Fig. 18B** and **Fig. S10B**), and

779   -6.0 and -16.2 ‰, respectively for $\beta_{Zr} = 0.113$ (Eq. 24; **Fig. 18C** and **Fig. S10C**). From Eq. 35,

780   we find that different Zr partition coefficients between minerals and melt K, different diffusive Zr

781   isotopic fractionation factor Δ_D (or the β_{Zr} exponent in Eq. 24), and different growth timescales

782   of the Zr-poor minerals result in a range of δ'^{94}Zr values of the liquid in the diffusive boundary

783   layer (see **Figs. 17, 18** and **Figs. S9, S10**) that can readily explain the values measured by Ibanez-

784   Meija and Tissot[66]. In **Fig. 19**, we plot the expected probability density function (PDF) of the Zr

785   isotopic composition of Zr atoms in the diffusive boundary layer (*i.e.*, at any given time, the

786   fraction of Zr atoms in the diffusive boundary layer with an enrichment higher than 3 that have a

787   certain isotopic composition) (movies **Mov. 9 and 10** are provided as Supporting Information).

788   We find more or less uniform distributions, while Ibanez-Meija and Tissot[66] found many zircons

789   with δ'^{94}Zr values around 0-1 ‰ and a long tail of δ'^{94}Zr values extending to -4 ‰. Comparing

35

790   these PDFs is, however, fraught with difficulties as there is no compelling reason to think that Zr

791   atoms in zircons reflect a snapshot of the diffusive boundary layer. If DTC is the correct model,

792   the distribution of δ'^{94}Zr values could help pinpoint when and where in the development of

793   diffusive boundary layers zircons can form.

794   While both positive and negative δ'^{94}Zr values are encountered in the diffusion boundary

795   layer considered in the DTC model (**Figs. 17, 18** and **Figs. S9, S10**), the distribution is skewed

796   towards low δ'^{94}Zr. This is also shown in **Fig. 19**, where we plot the average δ'^{94}Zr value of the

797   boundary layer where the melt is Zr-supersaturated by at least of factor of 3. The shift towards low

798   δ'^{94}Zr values in the boundary layer is due to the removal of isotopically heavy Zr in the growing

799   Zr-poor mineral (*e.g.*, clinopyroxene or plagioclase). At first sight, the development of low δ'^{94}Zr

800   values in zircons formed by DTC is consistent with the -0.5 ‰ δ'^{94}Zr fractionation calculated by

801   Inglis et al[64] for zircon in Hekla. However, for these zircons to drive Zr isotopic fractionation in

802   the magma, they would have to be separated from the Zr-poor minerals whose crystallization drove

803   zircon saturation, which may be difficult to achieve. Future studies investigating Zr-poor minerals

804   will help test if zircons formed around them were formed by diffusion-triggered crystallization.

805   To summarize, isotopic fractionation induced by diffusion in boundary layers around growing

806   Zr-poor crystals (DTC model) can readily explain the range of δ'^{94}Zr values measured in zircons.

807   An appealing aspect of this scenario is that the formation of a such a Zr-rich boundary layer could

808   also be the trigger for zircon saturation and crystallization. As with the DLC model outlined in

809   Sect. 4.3.1, the DTC model provides the framework to tie δ'^{94}Zr values measured in zircons to the

810   cooling history of the host magma.

811

812   **4.4. Combined Zr and Hf fractionations**

36

813   One manner to distinguish between equilibrium and kinetic isotopic fractionation is, in theory,

814   to compare $\delta'^{94}Zr$ and $\delta'^{179}Hf$. We performed *ab initio* calculations of the equilibrium

815   fractionation factor of Hf in a variety of minerals (**Fig. 4, Table 1**). Zirconium and hafnium form

816   bonds of similar strengths and as discussed in the results section, at equilibrium we expect the

817   isotopic fractionations of Zr and Hf between two phases A and B to scale as,

$$\frac{\Delta'^{94/90}Zr_{A-B}}{\Delta'^{179/177}Hf_{A-B}} \approx \frac{\left(\frac{1}{M^{90}}-\frac{1}{M^{94}}\right)}{\left(\frac{1}{M^{177}}-\frac{1}{M^{179}}\right)} = 7.5 \ . \tag{36}$$

819   Combining the diffusivity ratios of Zr and Hf isotopes (Eqs. 24 and 25), we expect to first-order

820   that kinetic isotopic fractionation induced by diffusion will produce isotopic fractionations for Zr

821   and Hf that scale as (see the formulas in Sio et al.[114,115]; Dauphas and Rouxel[133]; Watson and

822   Muller[132]; for a variety of diffusion geometries),

$$\frac{\delta'^{94/90}Zr}{\delta'^{179/177}Hf} \approx \frac{1-\frac{D^{94}}{D^{90}}}{1-\frac{D^{179}}{D^{177}}} \approx 3.8 \ . \tag{37}$$

824   This shows that equilibrium and diffusion-driven kinetic isotopic fractionation are expected to

825   produce very distinct $\frac{\delta'^{94}Zr}{\delta'^{179}Hf}$ values. No $\delta'^{179}Hf$ value has been reported but its combination with

826     $\delta'^{94}Zr$ measurements should provide a diagnostic tool to tell when Zr isotopic fractionation in

827   magmas reflects diffusive processes and use those effects to estimate the growth rate and cooling

828   history of zircons.

829

4.5. Potential usage in metamorphic zircons

831   Zirconium stable isotopic variations can potentially help unravel the complex processes

832   involved in metamorphic zircon formation. For example, our *ab initio* calculations show that under

833   amphibolite conditions (500-700 °C), Zr in amphibole should be fractionated in $\delta'^{94}Zr$ by 0.22-

37

834   0.35 ‰, or 0.55-0.86 ‰ relative to Zr in ilmenite (**Table 1**, we use tremolite to approximate the

835   fractionation in amphibole, the two ranges correspond to two substitution mechanisms for the

836   calculations of tremolite). It is thus conceivable that metamorphic zircon formed from the

837   decomposition of amphibole[147] would inherit the Zr isotopic composition of amphibole, which we

838   expect to be distinct from the Zr isotopic composition of the zircon formed by the breakdown of

839   ilmenite[148]. Inter-mineral fractionations between zircon and co-existing Zr-bearing metamorphic

840   minerals may also help recognizing equilibrium parageneses and inferring equilibration

841   temperatures.

842

843   **5. Conclusion**

844   This study presents first-principle calculations of equilibrium Zr and Hf isotopic fractionation

845   factors in a variety of Zr-rich phases as well as a large number of minerals where Zr is present at

846   trace level in substitution with other elements. The minerals studied include Ca-catapleiite, a

847   mineral that previous EXAFS studies showed contains Zr in a coordination environment similar

848   to that encountered in silicate melts. We find that in the temperature range relevant to magmatic

849   zircon crystallization, there is negligible equilibrium Zr isotopic fractionation between

850   zircon/baddeleyite and melt. In general, equilibrium Zr isotopic fractionation between silicate

851   minerals and melt is not significant either. Iron-titanium oxides (ilmenite and magnetite) have the

852   potential to produce non-negligible mass-dependent fractionation of Zr isotopes. However, we

853   show through modeling using Rhyolite-MELTS that the relatively low concentration of Zr in these

854   Fe,Ti-oxide mineral offers limited leverage to greatly modify the melt composition during

855   magmatic differentiation before zircon saturation.

856   Kinetic effects associated with diffusion-limited crystallization (DLC) of zircon can

857   potentially produce significant light Zr isotope enrichments in zircon. Reservoir effects in the

858   liquid would also lead to the crystallization of zircons with high δ'^{94}Zr. Diffusion-triggered

859   crystallization (DTC) of zircon from the diffusive boundary layer developed during the growth of

860   Zr-poor minerals can produce zircons with both positive and negative δ'^{94}Zr values. If diffusion-

861   driven kinetic effects are the main mechanism at play, Zr isotopic analyses of zircons would

862   provide a means of constraining the cooling history of the host magma. We show that correlating

863   Zr and Hf isotopic measurements can help identify kinetic effects in zircons, as equilibrium and

864   diffusive kinetic effects are expected to impart different correlations between δ'^{94}Zr and δ'^{179}Hf

865   values.

866

Supporting Information

867

868   (A) Derivation of diffusion-driven kinetic isotopic effects produced by the accumulation of an
869   incompatible element in a diffusive boundary layer.
870   (B) Supplementary Figures.
871   (C) Supplementary Tables.
872   (D) Titles and captions for every movie.
873   (E) Movies.
874

39

882

References

(1)   McDonough, W. F.; Sun, S.-S. The Composition of the Earth. *Chemical geology* **1995**, *120* (3–4), 223–253.

(2)   Rudnick, R.; Gao, S. Composition of the Continental Crust. *The crust* **2003**, *3*, 1–64.

(3)   Sohrin, Y.; Fujishima, Y.; Ueda, K.; Akiyama, S.; Mori, K.; Hasegawa, H.; Matsui, M. Dissolved Niobium and Tantalum in the North Pacific. *Geophysical research letters* **1998**, *25* (7), 999–1002.

(4)   Orians, K. J.; Boyle, E. A.; Bruland, K. W. Dissolved Titanium in the Open Ocean. *Nature* **1990**, *348* (6299), 322–325.

(5)   Lodders, K. Solar System Abundances and Condensation Temperatures of the Elements. *The Astrophysical Journal* **2003**, *591* (2), 1220.

(6)   Wood, B. J.; Smythe, D. J.; Harrison, T. The Condensation Temperatures of the Elements: A Reappraisal. *American Mineralogist: Journal of Earth and Planetary Materials* **2019**, *104* (6), 844–856.

(7)   Brimhall, G. H.; Dietrich, W. E. Constitutive Mass Balance Relations between Chemical Composition, Volume, Density, Porosity, and Strain in Metasomatic Hydrochemical Systems: Results on Weathering and Pedogenesis. *Geochimica et Cosmochimica Acta* **1987**, *51* (3), 567–587.

(8)   Sheldon, N. D.; Tabor, N. J. Quantitative Paleoenvironmental and Paleoclimatic Reconstruction Using Paleosols. *Earth-Science Reviews* **2009**, *95* (1–2), 1–52.

(9)   O'Neill, H. S. C.; Palme, H. Collisional Erosion and the Non-Chondritic Composition of the Terrestrial Planets. *Philosophical Transactions of the Royal Society A: Mathematical, Physical and Engineering Sciences* **2008**, *366* (1883), 4205–4238.

(10) Martin, P. M.; Mason, B. Major and Trace Elements in the Allende Meteorite. *Nature* **1974**, *249* (5455), 333–334.

(11) Grossman, L.; Ganapathy, R. Trace Elements in the Allende Meteorite—I. Coarse-Grained, Ca-Rich Inclusions. *Geochimica et Cosmochimica Acta* **1976**, *40* (3), 331–344.

(12) Grossman, L.; Ganapathy, R. Trace Elements in the Allende Meteorite—II. Fine-Grained. Ca-Rich Inclusions. *Geochimica et Cosmochimica Acta* **1976**, *40* (8), 967–977.

(13) MacPherson, G. J. Refractory Inclusions in the Prototypical CM Chondrite, Mighei. *Geochimica et Cosmochimica Acta* **1994**, *58* (24), 5599–5625.

(14) Simon, S. B.; Davis, A. M.; Grossman, L. A Unique Ultrarefractory Inclusion from the Murchison Meteorite. *Meteoritics & Planetary Science* **1996**, *31* (1), 106–115.

(15) El Goresy, A.; Zinner, E.; Matsunami, S.; Palme, H.; Spettel, B.; Lin, Y.; Nazarov, M. Efremovka 101.1: A CAI with Ultrarefractory REE Patterns and Enormous Enrichments of Sc, Zr, and Y in Fassaite and Perovskite. *Geochimica et Cosmochimica Acta* **2002**, *66* (8), 1459–1491.

(16) Vervoort, J.; Patchett, P.; Gehrels, G. E.; Nutman, A. Constraints on Early Earth Differentiation from Hafnium and Neodymium Isotopes. *Nature* **1996**, *379* (6566), 624–627.

(17) Blichert-Toft, J.; Albarède, F. The Lu-Hf Isotope Geochemistry of Chondrites and the Evolution of the Mantle-Crust System. *Earth and Planetary Science Letters* **1997**, *148* (1–2), 243–258.

40

926   (18)   Vervoort, J. D.; Blichert-Toft, J. Evolution of the Depleted Mantle: Hf Isotope Evidence
927   from Juvenile Rocks through Time. *Geochimica et cosmochimica acta* **1999**, *63* (3–4), 533–
928   556.
929   (19)   Harrison, T.; Blichert-Toft, J.; Müller, W.; Albarede, F.; Holden, P.; Mojzsis, S. J.
930   Heterogeneous Hadean Hafnium: Evidence of Continental Crust at 4.4 to 4.5 Ga. *Science*
931   **2005**, *310* (5756), 1947–1950.
932   (20)   Miyashiro, A.; Shido, F. Tholeiitic and Calc-Alkalic Series in Relation to the Behaviors of
933   Titanium, Vanadium, Chromium, and Nickel. *American Journal of Science* **1975**, *275* (3),
934   265–277.
935   (21)   Ross, P.-S.; Bédard, J. H. Magmatic Affinity of Modern and Ancient Subalkaline Volcanic
936   Rocks Determined from Trace-Element Discriminant Diagrams. *Canadian Journal of Earth
937   Sciences* **2009**, *46* (11), 823–839.
938   (22)   Wade, J.; Wood, B. The Earth's 'Missing'Niobium May Be in the Core. *Nature* **2001**, *409*
939   (6816), 75–78.
940   (23)   Rudnick, R. L.; Barth, M.; Horn, I.; McDonough, W. F. Rutile-Bearing Refractory Eclogites:
941   Missing Link between Continents and Depleted Mantle. *Science* **2000**, *287* (5451), 278–
942   281.
943   (24)   Münker, C.; Pfänder, J. A.; Weyer, S.; Büchl, A.; Kleine, T.; Mezger, K. Evolution of
944   Planetary Cores and the Earth-Moon System from Nb/Ta Systematics. *Science* **2003**, *301*
945   (5629), 84–87.
946   (25)   Pfänder, J. A.; Münker, C.; Stracke, A.; Mezger, K. Nb/Ta and Zr/Hf in Ocean Island
947   Basalts—Implications for Crust–Mantle Differentiation and the Fate of Niobium. *Earth and
948   Planetary Science Letters* **2007**, *254* (1–2), 158–172.
949   (26)   Pfänder, J. A.; Jung, S.; Münker, C.; Stracke, A.; Mezger, K. A Possible High Nb/Ta
950   Reservoir in the Continental Lithospheric Mantle and Consequences on the Global Nb
951   Budget–Evidence from Continental Basalts from Central Germany. *Geochimica et
952   Cosmochimica Acta* **2012**, *77*, 232–251.
953   (27)   Nebel, O.; van Westrenen, W.; Vroon, P. Z.; Wille, M.; Raith, M. M. Deep Mantle Storage
954   of the Earth's Missing Niobium in Late-Stage Residual Melts from a Magma Ocean.
955   *Geochimica et Cosmochimica Acta* **2010**, *74* (15), 4392–4404.
956   (28)   Jackson, M. G.; Hart, S. R.; Saal, A. E.; Shimizu, N.; Kurz, M. D.; Blusztajn, J. S.;
957   Skovgaard, A. C. Globally Elevated Titanium, Tantalum, and Niobium (TITAN) in Ocean
958   Island Basalts with High 3He/4He. *Geochemistry, Geophysics, Geosystems* **2008**, *9* (4).
959   (29)   Taylor, S. R.; McLennan, S. M. The Continental Crust: Its Composition and Evolution. **1985**.
960   (30)   Greber, N. D.; Dauphas, N. The Chemistry of Fine-Grained Terrigenous Sediments Reveals
961   a Chemically Evolved Paleoarchean Emerged Crust. *Geochimica et cosmochimica acta*
962   **2019**, *255*, 247–264.
963   (31)   Ptáček, M. P.; Dauphas, N.; Greber, N. D. Chemical Evolution of the Continental Crust
964   from a Data-Driven Inversion of Terrigenous Sediment Compositions. *Earth and planetary
965   science letters* **2020**, *539*, 116090.
966   (32)   Dauphas, N.; Schauble, E. A. Mass Fractionation Laws, Mass-Independent Effects, and
967   Isotopic Anomalies. *Annual Review of Earth and Planetary Sciences* **2016**, *44*, 709–783.
968   (33)   Niederer, F.; Papanastassiou, D.; Wasserburg, G. The Isotopic Composition of Titanium in
969   the Allende and Leoville Meteorites. *Geochimica et Cosmochimica Acta* **1981**, *45* (7),
970   1017–1031.

41

971 (34) Niemeyer, S.; Lugmair, G. Ubiquitous Isotopic Anomalies in Ti from Normal Allende
972   Inclusions. *Earth and Planetary Science Letters* **1981**, *53* (2), 211–225.

973 (35) Ireland, T.; Compston, W.; Heydegger, H. Titanium Isotopic Anomalies in Hibonites from
974   the Murchison Carbonaceous Chondrite. *Geochimica et Cosmochimica Acta* **1985**, *49* (9),
975   1989–1993.

976 (36) Zinner, E. K.; Fahey, A. J.; Goswami, J. N.; Ireland, T. R.; McKeegan, K. D. Large Ca-48
977   Anomalies Are Associated with Ti-50 Anomalies in Murchison and Murray Hibonites. *The
978   Astrophysical Journal* **1986**, *311*, L103–L107.

979 (37) Fahey, A.; Goswami, J.; McKeegan, K.; Zinner, E. 26Al, 244Pu, 50Ti, REE, and Trace
980   Element Abundances in Hibonite Grains from CM and CV Meteorites. *Geochimica et
981   Cosmochimica Acta* **1987**, *51* (2), 329–350.

982 (38) Trinquier, A.; Elliott, T.; Ulfbeck, D.; Coath, C.; Krot, A. N.; Bizzarro, M. Origin of
983   Nucleosynthetic Isotope Heterogeneity in the Solar Protoplanetary Disk. *Science* **2009**, *324*
984   (5925), 374–376.

985 (39) Zhang, J.; Dauphas, N.; Davis, A. M.; Pourmand, A. A New Method for MC-ICPMS
986   Measurement of Titanium Isotopic Composition: Identification of Correlated Isotope
987   Anomalies in Meteorites. *Journal of Analytical Atomic Spectrometry* **2011**, *26* (11), 2197–
988   2205.

989 (40) Leya, I.; Schönbächler, M.; Wiechert, U.; Krähenbühl, U.; Halliday, A. N. Titanium
990   Isotopes and the Radial Heterogeneity of the Solar System. *Earth and Planetary Science
991   Letters* **2008**, *266* (3–4), 233–244.

992 (41) Schönbächler, M.; Lee, D.-C.; Rehkämper, M.; Halliday, A. N.; Fehr, M. A.; Hattendorf,
993   B.; Günther, D. Zirconium Isotope Evidence for Incomplete Admixing of R-Process
994   Components in the Solar Nebula. *Earth and Planetary Science Letters* **2003**, *216* (4), 467–
995   481.

996 (42) Akram, W.; Schönbächler, M.; Sprung, P.; Vogel, N. Zirconium—Hafnium Isotope
997   Evidence from Meteorites for the Decoupled Synthesis of Light and Heavy Neutron-Rich
998   Nuclei. *The Astrophysical Journal* **2013**, *777* (2), 169.

999 (43) Akram, W.; Schönbächler, M.; Bisterzo, S.; Gallino, R. Zirconium Isotope Evidence for the
1000   Heterogeneous Distribution of S-Process Materials in the Solar System. *Geochimica et
1001   Cosmochimica Acta* **2015**, *165*, 484–500.

1002 (44) Peters, S. T.; Münker, C.; Pfeifer, M.; Elfers, B.-M.; Sprung, P. Distribution of P-Process
1003   174Hf in Early Solar System Materials and the Origin of Nucleosynthetic Hf and W Isotope
1004   Anomalies in Ca–Al Rich Inclusions. *Earth and Planetary Science Letters* **2017**, *459*, 70–
1005   79.

1006 (45) Elfers, B.-M.; Sprung, P.; Pfeifer, M.; Wombacher, F.; Peters, S. T.; Münker, C. Variable
1007   Distribution of S-Process Hf and W Isotope Carriers in Chondritic Meteorites–Evidence
1008   from 174Hf and 180W. *Geochimica et Cosmochimica Acta* **2018**, *239*, 346–362.

1009 (46) Elfers, B.-M.; Sprung, P.; Messling, N.; Münker, C. The Combined Zr and Hf Isotope
1010   Inventory of Bulk Rock and Sequentially Leached Chondrite Samples. *Geochimica et
1011   Cosmochimica Acta* **2020**, *270*, 475–491.

1012 (47) Zhang, J.; Dauphas, N.; Davis, A. M.; Leya, I.; Fedkin, A. The Proto-Earth as a Significant
1013   Source of Lunar Material. *Nature Geoscience* **2012**, *5* (4), 251–255.

1014 (48) Sprung, P.; Scherer, E. E.; Upadhyay, D.; Leya, I.; Mezger, K. Non-Nucleosynthetic
1015   Heterogeneity in Non-Radiogenic Stable Hf Isotopes: Implications for Early Solar System
1016   Chronology. *Earth and Planetary Science Letters* **2010**, *295* (1–2), 1–11.

42

1017   (49)   Sprung, P.; Kleine, T.; Scherer, E. E. Isotopic Evidence for Chondritic Lu/Hf and Sm/Nd of
1018   the Moon. *Earth and Planetary Science Letters* **2013**, *380*, 77–87.
1019   (50)   Harper Jr, C. L. Evidence for 92gNb in the Early Solar System and Evaluation of a New P-
1020   Process Cosmochronometer from 92gNb/92Mo. *The Astrophysical Journal* **1996**, *466*, 437.
1021   (51)   Schönbächler, M.; Rehkämper, M.; Halliday, A. N.; Lee, D.-C.; Bourot-Denise, M.; Zanda,
1022   B.; Hattendorf, B.; Günther, D. Niobium-Zirconium Chronometry and Early Solar System
1023   Development. *Science* **2002**, *295* (5560), 1705–1708.
1024   (52)   Iizuka, T.; Lai, Y.-J.; Akram, W.; Amelin, Y.; Schönbächler, M. The Initial Abundance and
1025   Distribution of 92Nb in the Solar System. *Earth and Planetary Science Letters* **2016**, *439*,
1026   172–181.
1027   (53)   Patchett, P.; Tatsumoto, M. Hafnium Isotope Variations in Oceanic Basalts. *Geophysical
1028   Research Letters* **1980**, *7* (12), 1077–1080.
1029   (54)   Patchett, P. J.; Kouvo, O.; Hedge, C. E.; Tatsumoto, M. Evolution of Continental Crust and
1030   Mantle Heterogeneity: Evidence from Hf Isotopes. *Contributions to Mineralogy and
1031   Petrology* **1982**, *78* (3), 279–297.
1032   (55)   Millet, M.-A.; Dauphas, N.; Greber, N. D.; Burton, K. W.; Dale, C. W.; Debret, B.;
1033   Macpherson, C. G.; Nowell, G. M.; Williams, H. M. Titanium Stable Isotope Investigation
1034   of Magmatic Processes on the Earth and Moon. *Earth and planetary science letters* **2016**,
1035   *449*, 197–205.
1036   (56)   Greber, N. D.; Dauphas, N.; Puchtel, I. S.; Hofmann, B. A.; Arndt, N. T. Titanium Stable
1037   Isotopic Variations in Chondrites, Achondrites and Lunar Rocks. *Geochimica et
1038   cosmochimica acta* **2017**, *213*, 534–552.
1039   (57)   Greber, N. D.; Dauphas, N.; Bekker, A.; Ptáček, M. P.; Bindeman, I. N.; Hofmann, A.
1040   Titanium Isotopic Evidence for Felsic Crust and Plate Tectonics 3.5 Billion Years Ago.
1041   *Science* **2017**, *357* (6357), 1271–1274.
1042   (58)   Simon, J.; Jordan, M.; Tappa, M.; Schauble, E.; Kohl, I.; Young, E. Calcium and Titanium
1043   Isotope Fractionation in Refractory Inclusions: Tracers of Condensation and Inheritance in
1044   the Early Solar Protoplanetary Disk. *Earth and Planetary Science Letters* **2017**, *472*, 277–
1045   288.
1046   (59)   Davis, A. M.; Zhang, J.; Greber, N. D.; Hu, J.; Tissot, F. L.; Dauphas, N. Titanium Isotopes
1047   and Rare Earth Patterns in CAIs: Evidence for Thermal Processing and Gas-Dust
1048   Decoupling in the Protoplanetary Disk. *Geochimica et cosmochimica acta* **2018**, *221*, 275–
1049   295.
1050   (60)   Deng, Z.; Moynier, F.; Sossi, P.; Chaussidon, M. Bridging the Depleted MORB Mantle and
1051   the Continental Crust Using Titanium Isotopes. **2018**.
1052   (61)   Deng, Z.; Chaussidon, M.; Savage, P.; Robert, F.; Pik, R.; Moynier, F. Titanium Isotopes as
1053   a Tracer for the Plume or Island Arc Affinity of Felsic Rocks. *Proceedings of the National
1054   Academy of Sciences* **2019**, *116* (4), 1132–1135.
1055   (62)   Johnson, A. C.; Aarons, S. M.; Dauphas, N.; Nie, N. X.; Zeng, H.; Helz, R. T.; Romaniello,
1056   S. J.; Anbar, A. D. Titanium Isotopic Fractionation in Kilauea Iki Lava Lake Driven by
1057   Oxide Crystallization. *Geochimica et Cosmochimica Acta* **2019**, *264*, 180–190.
1058   (63)   Inglis, E. C.; Creech, J. B.; Deng, Z.; Moynier, F. High-Precision Zirconium Stable Isotope
1059   Measurements of Geological Reference Materials as Measured by Double-Spike MC-
1060   ICPMS. *Chemical Geology* **2018**, *493*, 544–552.
1061   (64)   Inglis, E. C.; Moynier, F.; Creech, J.; Deng, Z.; Day, J. M.; Teng, F.-Z.; Bizzarro, M.;
1062   Jackson, M.; Savage, P. Isotopic Fractionation of Zirconium during Magmatic

Differentiation and the Stable Isotope Composition of the Silicate Earth. *Geochimica et Cosmochimica Acta* **2019**, *250*, 311–323.

(65)   Zhang, W.; Wang, Z.; Moynier, F.; Inglis, E.; Tian, S.; Li, M.; Liu, Y.; Hu, Z. Determination of Zr Isotopic Ratios in Zircons Using Laser-Ablation Multiple-Collector Inductively Coupled-Plasma Mass-Spectrometry. *Journal of Analytical Atomic Spectrometry* **2019**, *34* (9), 1800–1809.

(66)   Ibañez-Mejia, M.; Tissot, F. L. Extreme Zr Stable Isotope Fractionation during Magmatic Fractional Crystallization. *Science Advances* **2019**, *5* (12), eaax8648.

(67)   Feng, L.; Hu, W.; Jiao, Y.; Zhou, L.; Zhang, W.; Hu, Z.; Liu, Y. High-Precision Stable Zirconium Isotope Ratio Measurements by Double Spike Thermal Ionization Mass Spectrometry. *Journal of Analytical Atomic Spectrometry* **2020**, *35* (4), 736–745.

(68)   Tompkins, H. G.; Zieman, L. J.; Ibañez-Mejia, M.; Tissot, F. L. Zirconium Stable Isotope Analysis of Zircon by MC-ICP-MS: Methods and Application to Evaluating Intra-Crystalline Zonation in a Zircon Megacryst. *Journal of Analytical Atomic Spectrometry* **2020**.

(69)   Tian, S.; Inglis, E.; Creech, J.; Zhang, W.; Wang, Z.; Hu, Z.; Liu, Y.; Moynier, F. The Zirconium Stable Isotope Compositions of 22 Geological Reference Materials, 4 Zircons and 3 Standard Solutions. *Chemical Geology* **2020**, 119791.

(70)   Wang, W.; Huang, S.; Huang, F.; Zhao, X.; Wu, Z. Equilibrium Inter-Mineral Titanium Isotope Fractionation: Implication for High-Temperature Titanium Isotope Geochemistry. *Geochimica et Cosmochimica Acta* **2020**, *269*, 540–553.

(71)   Bowring, S. A.; Erwin, D.; Jin, Y.; Martin, M.; Davidek, K.; Wang, W. U/Pb Zircon Geochronology and Tempo of the End-Permian Mass Extinction. *Science* **1998**, *280* (5366), 1039–1045.

(72)   Amelin, Y.; Lee, D.-C.; Halliday, A. N.; Pidgeon, R. T. Nature of the Earth's Earliest Crust from Hafnium Isotopes in Single Detrital Zircons. *Nature* **1999**, *399* (6733), 252–255.

(73)   Mojzsis, S. J.; Harrison, T. M.; Pidgeon, R. T. Oxygen-Isotope Evidence from Ancient Zircons for Liquid Water at the Earth's Surface 4,300 Myr Ago. *Nature* **2001**, *409* (6817), 178–181.

(74)   Wilde, S. A.; Valley, J. W.; Peck, W. H.; Graham, C. M. Evidence from Detrital Zircons for the Existence of Continental Crust and Oceans on the Earth 4.4 Gyr Ago. *Nature* **2001**, *409* (6817), 175–178.

(75)   Watson, E. B.; Harrison, T. Zircon Thermometer Reveals Minimum Melting Conditions on Earliest Earth. *Science* **2005**, *308* (5723), 841–844.

(76)   Valley, J.; Lackey, J.; Cavosie, A.; Clechenko, C.; Spicuzza, M.; Basei, M.; Bindeman, I.; Ferreira, V.; Sial, A.; King, E. 4.4 Billion Years of Crustal Maturation: Oxygen Isotope Ratios of Magmatic Zircon. *Contributions to Mineralogy and Petrology* **2005**, *150* (6), 561–580.

(77)   Hopkins, M.; Harrison, T. M.; Manning, C. E. Low Heat Flow Inferred From> 4 Gyr Zircons Suggests Hadean Plate Boundary Interactions. *Nature* **2008**, *456* (7221), 493–496.

(78)   Hawkesworth, C. J.; Dhuime, B.; Pietranik, A.; Cawood, P.; Kemp, A. I.; Storey, C. The Generation and Evolution of the Continental Crust. *Journal of the Geological Society* **2010**, *167* (2), 229–248.

(79)   Schoene, B.; Eddy, M. P.; Samperton, K. M.; Keller, C. B.; Keller, G.; Adatte, T.; Khadri, S. F. U-Pb Constraints on Pulsed Eruption of the Deccan Traps across the End-Cretaceous Mass Extinction. *Science* **2019**, *363* (6429), 862–866.

44

1109   (80)   Farges, F.; Ponader, C. W.; Brown Jr, G. E. Structural Environments of Incompatible
1110   Elements in Silicate Glass/Melt Systems: I. Zirconium at Trace Levels. *Geochimica et*
1111   *Cosmochimica Acta* **1991**, *55* (6), 1563–1574.
1112   (81)   Bigeleisen, J.; Mayer, M. G. Calculation of Equilibrium Constants for Isotopic Exchange
1113   Reactions.   *The   Journal   of   Chemical   Physics*   **1947**,   *15*   (5),   261.
1114   https://doi.org/10.1063/1.1746492.
1115   (82)   Urey, H. C. The Thermodynamic Properties of Isotopic Substances. *Journal of the Chemical*
1116   *Society (Resumed)* **1947**, No. 582, 562. https://doi.org/10.1039/jr9470000562.
1117   (83)   Polyakov, V.; Mineev, S.; Clayton, R.; Hu, G.; Gurevich, V.; Khramov, D.; Gavrichev, K.;
1118   Gorbunov, V.; Golushina, L. Oxygen Isotope Fractionation Factors Involving Cassiterite
1119   (SnO2): I. Calculation of Reduced Partition Function Ratios from Heat Capacity and X-Ray
1120   Resonant Studies. *Geochimica et cosmochimica acta* **2005**, *69* (5), 1287–1300.
1121   (84)   Dauphas, N.; Roskosz, M.; Alp, E.; Golden, D.; Sio, C.; Tissot, F.; Hu, M.; Zhao, J.; Gao,
1122   L.; Morris, R. A General Moment NRIXS Approach to the Determination of Equilibrium
1123   Fe Isotopic Fractionation Factors: Application to Goethite and Jarosite. *Geochimica et*
1124   *Cosmochimica Acta* **2012**, *94*, 254–275.
1125   (85)   Herzfeld, K. F.; Teller, E. The Vapor Pressure of Isotopes. *Physical Review* **1938**, *54* (11),
1126   912.
1127   (86)   Bigeleisen, J.; Mayer, M. G. Calculation of Equilibrium Constants for Isotopic Exchange
1128   Reactions. *The Journal of Chemical Physics* **1947**, *15* (5), 261–267.
1129   (87)   Dauphas, N.; Hu, M. Y.; Baker, E. M.; Hu, J.; Tissot, F. L.; Alp, E. E.; Roskosz, M.; Zhao,
1130   J.; Bi, W.; Liu, J. SciPhon: A Data Analysis Software for Nuclear Resonant Inelastic X-Ray
1131   Scattering with Applications to Fe, Kr, Sn, Eu and Dy. *Journal of synchrotron radiation*
1132   **2018**, *25* (5), 1581–1599.
1133   (88)   Blanchard, M.; Dauphas, N.; Hu, M.; Roskosz, M.; Alp, E.; Golden, D.; Sio, C.; Tissot, F.;
1134   Zhao, J.; Gao, L. Reduced Partition Function Ratios of Iron and Oxygen in Goethite.
1135   *Geochimica et Cosmochimica Acta* **2015**, *151*, 19–33.
1136   (89)   Yang, H.; Lin, J.-F.; Hu, M. Y.; Roskosz, M.; Bi, W.; Zhao, J.; Alp, E. E.; Liu, J.; Liu, J.;
1137   Wentzcovitch, R. M. Iron Isotopic Fractionation in Mineral Phases from Earth's Lower
1138   Mantle: Did Terrestrial Magma Ocean Crystallization Fractionate Iron Isotopes? *Earth and*
1139   *Planetary Science Letters* **2019**, *506*, 113–122.
1140   (90)   Zeng, H.; Rozsa, V. F.; Nie, N. X.; Zhang, Z.; Pham, T. A.; Galli, G.; Dauphas, N. Ab Initio
1141   Calculation of Equilibrium Isotopic Fractionations of Potassium and Rubidium in Minerals
1142   and Water. *ACS Earth and Space Chemistry* **2019**, *3* (11), 2601–2612.
1143   (91)   Roskosz, M.; Amet, Q.; Fitoussi, C.; Dauphas, N.; Bourdon, B.; Tissandier, L.; Hu, M.; Said,
1144   A.; Alatas, A.; Alp, E. Redox and Structural Controls on Tin Isotopic Fractionations among
1145   Magmas. *Geochimica et Cosmochimica Acta* **2020**, *268*, 42–55.
1146   (92)   Blöchl, P. E. Projector Augmented-Wave Method. *Physical Review B* **1994**, *50* (24), 17953–
1147   17979. https://doi.org/10.1103/PhysRevB.50.17953.
1148   (93)   Perdew, J. P.; Burke, K.; Ernzerhof, M. Generalized Gradient Approximation Made Simple.
1149   *Physical   Review   Letters*   **1996**,   *77*   (18),   3865–3868.
1150   https://doi.org/10.1103/PhysRevLett.77.3865.
1151   (94)   Togo, A.; Tanaka, I. First Principles Phonon Calculations in Materials Science. *Scripta*
1152   *Materialia* **2015**, *108*, 1–5. https://doi.org/10.1016/j.scriptamat.2015.07.021.
1153   (95)   Alfe, D.; Price, G. D.; Gillan, M. J. Oxygen in the Earth's Core: A First-Principles Study.
1154   *Physics of the Earth and Planetary Interiors* **1999**, *110* (3–4), 191–210.

45

1155 (96) Stixrude, L.; Karki, B. Structure and Freezing of MgSiO3 Liquid in Earth's Lower Mantle.
1156   *Science* **2005**, *310* (5746), 297–299.
1157 (97) Solomatova, N.; Caracas, R. Pressure-induced Coordination Changes in a Pyrolitic Silicate
1158   Melt from Ab Initio Molecular Dynamics Simulations. *Journal of Geophysical Research:*
1159   *Solid Earth* **2019**, *124* (11), 11232–11250.
1160 (98) Huang, D.; Badro, J.; Brodholt, J.; Li, Y. Ab Initio Molecular Dynamics Investigation of
1161   Molten Fe–Si–O in Earth's Core. *Geophysical Research Letters* **2019**, *46* (12), 6397–6405.
1162 (99) Stavros, F.; Yang, A.; Leon, A.; Nuttall, M.; Rasmussen, H. S. Characterization of Structure
1163   and Function of ZS-9, a K+ Selective Ion Trap. *PLoS One* **2014**, *9* (12), e114686.
1164 (100) Keyser, D. J.; Guillem, A. F. Microporous Zirconium Silicate for the Treatment of
1165   Hyperkalemia. **2014**.
1166 (101) Eggins, S.; Rudnick, R.; McDonough, W. The Composition of Peridotites and Their
1167   Minerals: A Laser-Ablation ICP–MS Study. *Earth and planetary science letters* **1998**, *154*
1168   (1–4), 53–71.
1169 (102) Ionov, D. Chemical Variations in Peridotite Xenoliths from Vitim, Siberia: Inferences for
1170   REE and Hf Behaviour in the Garnet-Facies Upper Mantle. *Journal of Petrology* **2004**, *45*
1171   (2), 343–367.
1172 (103) Farges, F.; Brown, G. E.; Velde, D. Structural Environment of Zr in Two Inosilicates from
1173   Cameroon: Mineralogical and Geochemical Implications. *American Mineralogist* **1994**, *79*
1174   (9–10), 838–847.
1175 (104) Smirnov, V.; Antonova, O.; Smirnov, S.; Goldberg, M.; Komlev, V.; Barinov, S. Effect of
1176   Titanium and Zirconium Substitutions for Calcium on the Formation and Structure of
1177   Tricalcium Phosphate and Hydroxyapatite. *Inorganic Materials* **2017**, *53* (12), 1254–1260.
1178 (105) Huang, F.; Chen, L.; Wu, Z.; Wang, W. First-Principles Calculations of Equilibrium Mg
1179   Isotope Fractionations between Garnet, Clinopyroxene, Orthopyroxene, and Olivine:
1180   Implications for Mg Isotope Thermometry. *Earth and Planetary Science Letters* **2013**, *367*,
1181   61–70. https://doi.org/10.1016/j.epsl.2013.02.025.
1182 (106) Wang, W.; Qin, T.; Zhou, C.; Huang, S.; Wu, Z.; Huang, F. Concentration Effect on
1183   Equilibrium Fractionation of Mg-Ca Isotopes in Carbonate Minerals: Insights from First-
1184   Principles Calculations. *Geochimica et Cosmochimica Acta* **2017**, *208*, 185–197.
1185   https://doi.org/10.1016/j.gca.2017.03.023.
1186 (107) Wang, W.; Zhou, C.; Liu, Y.; Wu, Z.; Huang, F. Equilibrium Mg Isotope Fractionation
1187   among Aqueous Mg2+, Carbonates, Brucite and Lizardite: Insights from First-Principles
1188   Molecular Dynamics Simulations. *Geochimica et Cosmochimica Acta* **2019**, *250*, 117–129.
1189   https://doi.org/10.1016/j.gca.2019.01.042.
1190 (108) Schauble, E. A. First-Principles Estimates of Equilibrium Magnesium Isotope Fractionation
1191   in Silicate, Oxide, Carbonate and Hexaaquamagnesium(2+) Crystals. *Geochimica et*
1192   *Cosmochimica Acta* **2011**, *75* (3), 844–869. https://doi.org/10.1016/j.gca.2010.09.044.
1193 (109) Méheut, M.; Lazzeri, M.; Balan, E.; Mauri, F. Structural Control over Equilibrium Silicon
1194   and Oxygen Isotopic Fractionation: A First-Principles Density-Functional Theory Study.
1195   *Chemical Geology* **2009**, *258* (1–2), 28–37. https://doi.org/10.1016/j.chemgeo.2008.06.051.
1196 (110) Schauble, E. A. Applying Stable Isotope Fractionation Theory to New Systems. *Reviews in*
1197   *Mineralogy and Geochemistry* **2004**, *55* (1), 65–111.
1198 (111) Dauphas, N.; John, S. G.; Rouxel, O. Iron Isotope Systematics. *Reviews in Mineralogy and*
1199   *Geochemistry* **2017**, *82* (1), 415–510.

46

(112) Dauphas, N.; Teng, F.-Z.; Arndt, N. T. Magnesium and Iron Isotopes in 2.7 Ga Alexo Komatiites: Mantle Signatures, No Evidence for Soret Diffusion, and Identification of Diffusive Transport in Zoned Olivine. *Geochimica et Cosmochimica Acta* **2010**, *74* (11), 3274–3291.

(113) Teng, F.-Z.; Dauphas, N.; Helz, R. T.; Gao, S.; Huang, S. Diffusion-Driven Magnesium and Iron Isotope Fractionation in Hawaiian Olivine. *Earth and Planetary Science Letters* **2011**, *308* (3–4), 317–324.

(114) Sio, C. K. I.; Dauphas, N.; Teng, F.-Z.; Chaussidon, M.; Helz, R. T.; Roskosz, M. Discerning Crystal Growth from Diffusion Profiles in Zoned Olivine by in Situ Mg–Fe Isotopic Analyses. *Geochimica et Cosmochimica Acta* **2013**, *123*, 302–321.

(115) Kin I Sio, C.; Dauphas, N. Thermal and Crystallization Histories of Magmatic Bodies by Monte Carlo Inversion of Mg-Fe Isotopic Profiles in Olivine. *Geology* **2017**, *45* (1), 67–70.

(116) Oeser, M.; Dohmen, R.; Horn, I.; Schuth, S.; Weyer, S. Processes and Time Scales of Magmatic Evolution as Revealed by Fe–Mg Chemical and Isotopic Zoning in Natural Olivines. *Geochimica et Cosmochimica Acta* **2015**, *154*, 130–150.

(117) Claiborne, L. L.; Miller, C.; Walker, B.; Wooden, J.; Mazdab, F.; Bea, F. Tracking Magmatic Processes through Zr/Hf Ratios in Rocks and Hf and Ti Zoning in Zircons: An Example from the Spirit Mountain Batholith, Nevada. *Mineralogical Magazine* **2006**, *70* (5), 517–543.

(118) Claiborne, L. L.; Miller, C. F.; Wooden, J. L. Trace Element Composition of Igneous Zircon: A Thermal and Compositional Record of the Accumulation and Evolution of a Large Silicic Batholith, Spirit Mountain, Nevada. *Contributions to Mineralogy and Petrology* **2010**, *160* (4), 511–531.

(119) Padilla, A.; Miller, C.; Carley, T.; Economos, R.; Schmitt, A.; Coble, M.; Wooden, J.; Fisher, C.; Vervoort, J.; Hanchar, J. Elucidating the Magmatic History of the Austurhorn Silicic Intrusive Complex (Southeast Iceland) Using Zircon Elemental and Isotopic Geochemistry and Geochronology. *Contributions to Mineralogy and Petrology* **2016**, *171* (8–9), 69.

(120) Aranovich, L. Y.; Bortnikov, N. New Zr–Hf Geothermometer for Magmatic Zircons. *Petrology* **2018**, *26* (2), 115–120.

(121) Gualda, G. A.; Ghiorso, M. S.; Lemons, R. V.; Carley, T. L. Rhyolite-MELTS: A Modified Calibration of MELTS Optimized for Silica-Rich, Fluid-Bearing Magmatic Systems. *Journal of Petrology* **2012**, *53* (5), 875–890.

(122) Watson, E. B.; Harrison, T. M. Zircon Saturation Revisited: Temperature and Composition Effects in a Variety of Crustal Magma Types. *Earth and Planetary Science Letters* **1983**, *64* (2), 295–304.

(123) Boehnke, P.; Watson, E. B.; Trail, D.; Harrison, T. M.; Schmitt, A. K. Zircon Saturation Re-Revisited. *Chemical Geology* **2013**, *351*, 324–334.

(124) Helz, R. T.; Kirschenbaum, H.; Marinenko, J.; Qian, R. *Whole-Rock Analyses of Core Samples from the 1967, 1975, 1979 and 1981 Drillings of Kilauea Iki Lava Lake, Hawaii*; 2331–1258; US Geological Survey, 1994.

(125) Grove, T. L.; Baker, M. B. Phase Equilibrium Controls on the Tholeiitic versus Calc-alkaline Differentiation Trends. *Journal of Geophysical Research: Solid Earth* **1984**, *89* (B5), 3253–3274.

(126) Juster, T. C.; Grove, T. L.; Perfit, M. R. Experimental Constraints on the Generation of FeTi Basalts, Andesites, and Rhyodacites at the Galapagos Spreading Center, 85 W and 95 W. *Journal of Geophysical Research: Solid Earth* **1989**, *94* (B7), 9251–9274.

47

(127) Sisson, T.; Grove, T. Experimental Investigations of the Role of H 2 O in Calc-Alkaline Differentiation and Subduction Zone Magmatism. *Contributions to mineralogy and petrology* **1993**, *113* (2), 143–166.

(128) Grove, T. L.; Elkins-Tanton, L. T.; Parman, S. W.; Chatterjee, N.; Müntener, O.; Gaetani, G. A. Fractional Crystallization and Mantle-Melting Controls on Calc-Alkaline Differentiation Trends. *Contributions to Mineralogy and Petrology* **2003**, *145* (5), 515–533.

(129) Richter, F. M.; Watson, E. B.; Mendybaev, R.; Dauphas, N.; Georg, B.; Watkins, J.; Valley, J. Isotopic Fractionation of the Major Elements of Molten Basalt by Chemical and Thermal Diffusion. *Geochimica et Cosmochimica Acta* **2009**, *73* (14), 4250–4263.

(130) Chopra, R.; Richter, F. M.; Watson, E. B.; Scullard, C. R. Magnesium Isotope Fractionation by Chemical Diffusion in Natural Settings and in Laboratory Analogues. *Geochimica et Cosmochimica Acta* **2012**, *88*, 1–18.

(131) Jambon, A. Isotopic Fractionation: A Kinetic Model for Crystals Growing from Magmatic Melts. *Geochimica et Cosmochimica Acta* **1980**, *44* (9), 1373–1380.

(132) Watson, E. B.; Müller, T. Non-Equilibrium Isotopic and Elemental Fractionation during Diffusion-Controlled Crystal Growth under Static and Dynamic Conditions. *Chemical Geology* **2009**, *267* (3–4), 111–124.

(133) Dauphas, N.; Rouxel, O. Mass Spectrometry and Natural Variations of Iron Isotopes. *Mass Spectrometry Reviews* **2006**, *25* (4), 515–550.

(134) DePaolo, D. J. Surface Kinetic Model for Isotopic and Trace Element Fractionation during Precipitation of Calcite from Aqueous Solutions. *Geochimica et cosmochimica acta* **2011**, *75* (4), 1039–1056.

(135) Richter, F. M.; Davis, A. M.; DePaolo, D. J.; Watson, E. B. Isotope Fractionation by Chemical Diffusion between Molten Basalt and Rhyolite. *Geochimica et Cosmochimica Acta* **2003**, *67* (20), 3905–3923.

(136) Richter, F. M.; Watson, E. B.; Mendybaev, R. A.; Teng, F.-Z.; Janney, P. E. Magnesium Isotope Fractionation in Silicate Melts by Chemical and Thermal Diffusion. *Geochimica et Cosmochimica Acta* **2008**, *72* (1), 206–220.

(137) Watkins, J. M.; DePaolo, D. J.; Huber, C.; Ryerson, F. J. Liquid Composition-Dependence of Calcium Isotope Fractionation during Diffusion in Molten Silicates. *Geochimica et Cosmochimica Acta* **2009**, *73* (24), 7341–7359.

(138) Watkins, J. M.; DePaolo, D. J.; Ryerson, F. J.; Peterson, B. T. Influence of Liquid Structure on Diffusive Isotope Separation in Molten Silicates and Aqueous Solutions. *Geochimica et Cosmochimica Acta* **2011**, *75* (11), 3103–3118.

(139) Watkins, J. M.; Liang, Y.; Richter, F.; Ryerson, F. J.; DePaolo, D. J. Diffusion of Multi-Isotopic Chemical Species in Molten Silicates. *Geochimica et Cosmochimica Acta* **2014**, *139*, 313–326.

(140) Watkins, J. M.; DePaolo, D. J.; Watson, E. B. Kinetic Fractionation of Non-Traditional Stable Isotopes by Diffusion and Crystal Growth Reactions. *Reviews in Mineralogy and Geochemistry* **2017**, *82* (1), 85–125.

(141) Zhang, Y.; Ni, H.; Chen, Y. Diffusion Data in Silicate Melts. *Reviews in Mineralogy and Geochemistry* **2010**, *72* (1), 311–408.

(142) Zhang, Y.; Xu, Z. Zircon Saturation and Zr Diffusion in Rhyolitic Melts, and Zircon Growth Geospeedometer. *American Mineralogist* **2016**, *101* (6), 1252–1267.

48

(143) Bindeman, I. N.; Melnik, O. E. Zircon Survival, Rebirth and Recycling during Crustal Melting, Magma Crystallization, and Mixing Based on Numerical Modelling. *Journal of Petrology* **2016**, *57* (3), 437–460.

(144) Carley, T. L.; Miller, C. F.; Wooden, J. L.; Bindeman, I. N.; Barth, A. P. Zircon from Historic Eruptions in Iceland: Reconstructing Storage and Evolution of Silicic Magmas. *Mineralogy and Petrology* **2011**, *102* (1–4), 135.

(145) Harrison, T. M.; Watson, E. B. The Behavior of Apatite during Crustal Anatexis: Equilibrium and Kinetic Considerations. *Geochimica et Cosmochimica Acta* **1984**, *48* (7), 1467–1477.

(146) Smith, V. G.; Tiller, W. A.; Rutter, J. A Mathematical Analysis of Solute Redistribution during Solidification. *Canadian Journal of Physics* **1955**, *33* (12), 723–745.

(147) Fraser, G.; Ellis, D.; Eggins, S. Zirconium Abundance in Granulite-Facies Minerals, with Implications for Zircon Geochronology in High-Grade Rocks. *Geology* **1997**, *25* (7), 607–610.

(148) Bingen, B.; Austrheim, H.; Whitehouse, M. Ilmenite as a Source for Zirconium during High-Grade Metamorphism? Textural Evidence from the Caledonides of Western Norway and Implications for Zircon Geochronology. *Journal of Petrology* **2001**, *42* (2), 355–375.

Figures and Tables
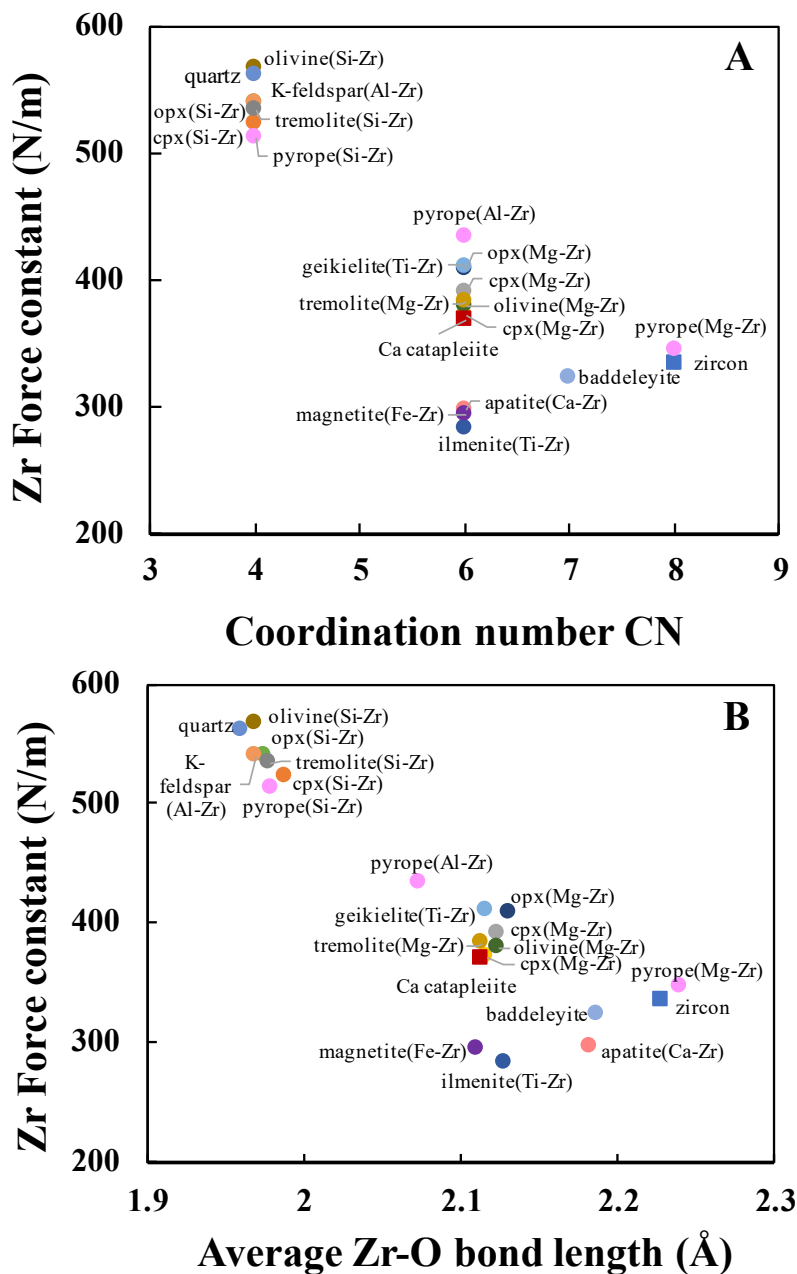
Figure 1. (A) Zr mean force constant (N/m) as a function of Zr coordination number in minerals calculated in this study. Lower coordination number generally corresponds to higher force constant (stronger bond). (B) Zr mean force constant (N/m) as a function of Zr-O bond length (Å). Shorter Zr-O bond length generally corresponds to stronger bond.
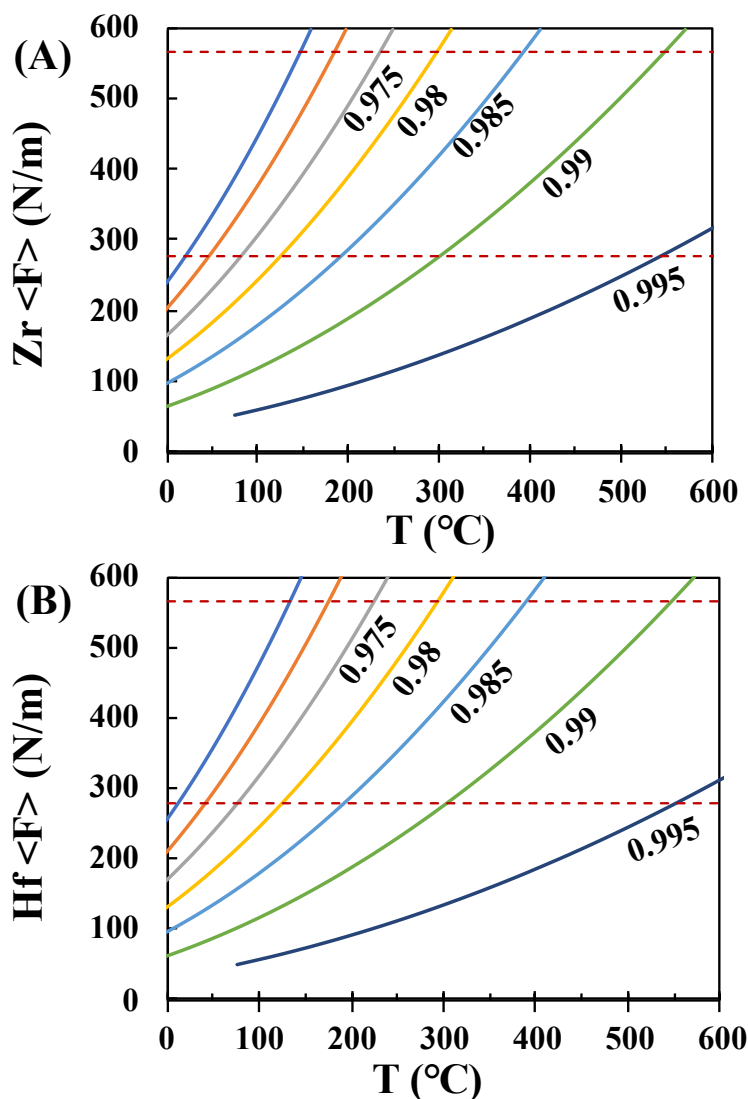
Figure 2. Relative error in the high temperature approximation $1000ln\beta = B_1\langle F\rangle/T^2$ (Eqs. 6, 7) calculated using the 1-parameter 3-term expansion $1000ln\beta = B_1\langle F\rangle/T^2 + B_2\langle F\rangle^2/T^4 + B_3\langle F\rangle^3/T^6$ (Eqs. 10, 12). The curves were calculated following Dauphas et al.[84] for different values of T and $\langle F\rangle$. (A) Relative departure from Eq. (10) when truncating the polynomial to the first order for Zr. The force constants of Zr bonds in all calculated minerals are between 280 and 566 N/m (red dashed lines). When the temperature is higher than ~300-500 °C, truncating the expansion to the first order (Eq. 6) will give a $1000ln\beta$ value that is within 1% of the value given by the whole expansion (Eq. 4). (B) Relative departure from Eq. (12) when truncating the polynomial to the first order for Hf. When the temperature is higher than ~300-500 °C, truncating the expansion to the first order (Eq. 7) will give a $1000ln\beta$ value that is within 1% of the value given by the whole expansion (Eq. 4). The high temperature approximation can be applied to calculate equilibrium Zr and Hf isotopic fractionation in igneous and metamorphic geochemistry/petrology without compromising accuracy.

51
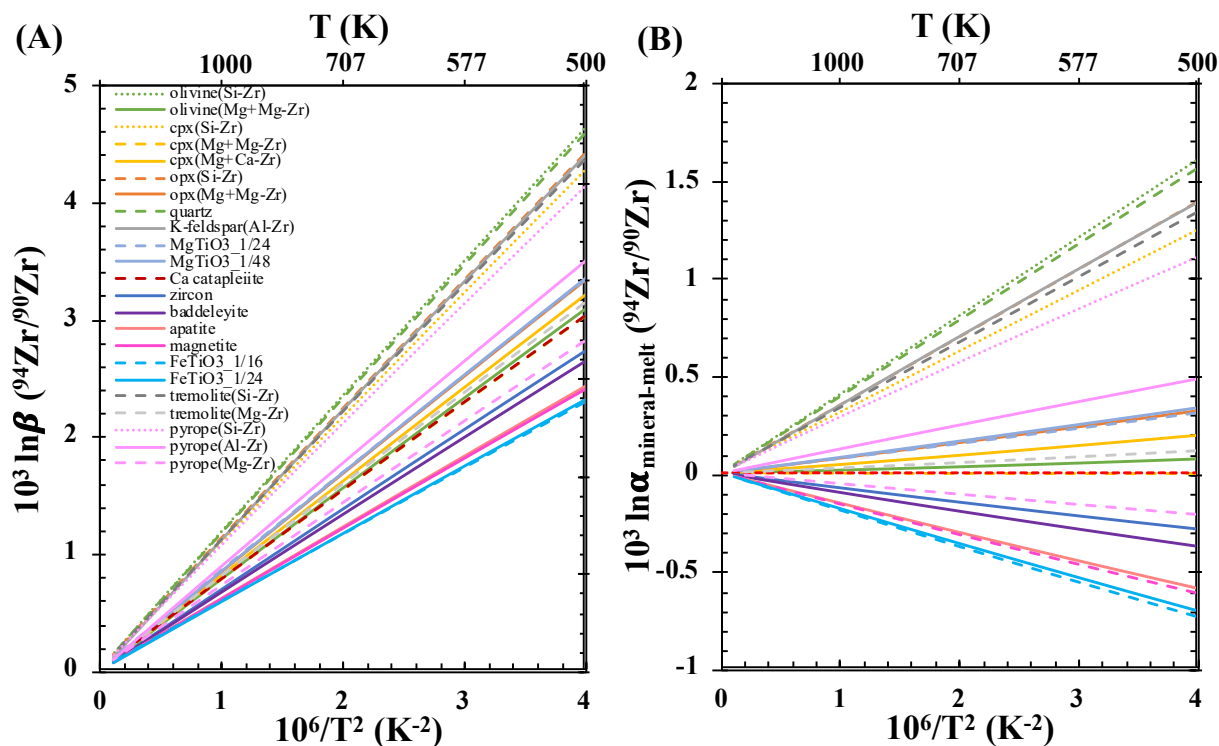
Figure 3. (A) Temperature-dependent 1000lnβ for Zr isotopes in minerals investigated in this study. (B) Temperature-dependent 1000lnα$_{mineral-melt}$ for Zr isotopes in the same set of minerals. The fractionation factors between minerals and melt are calculated by taking the difference between each mineral and Ca-catapleiite (which we use as silicate melt proxy). The calculation results for minerals with different Zr substitution mechanisms as well as different Zr concentrations are also shown in the figure. See main text and **Table 1** for details.
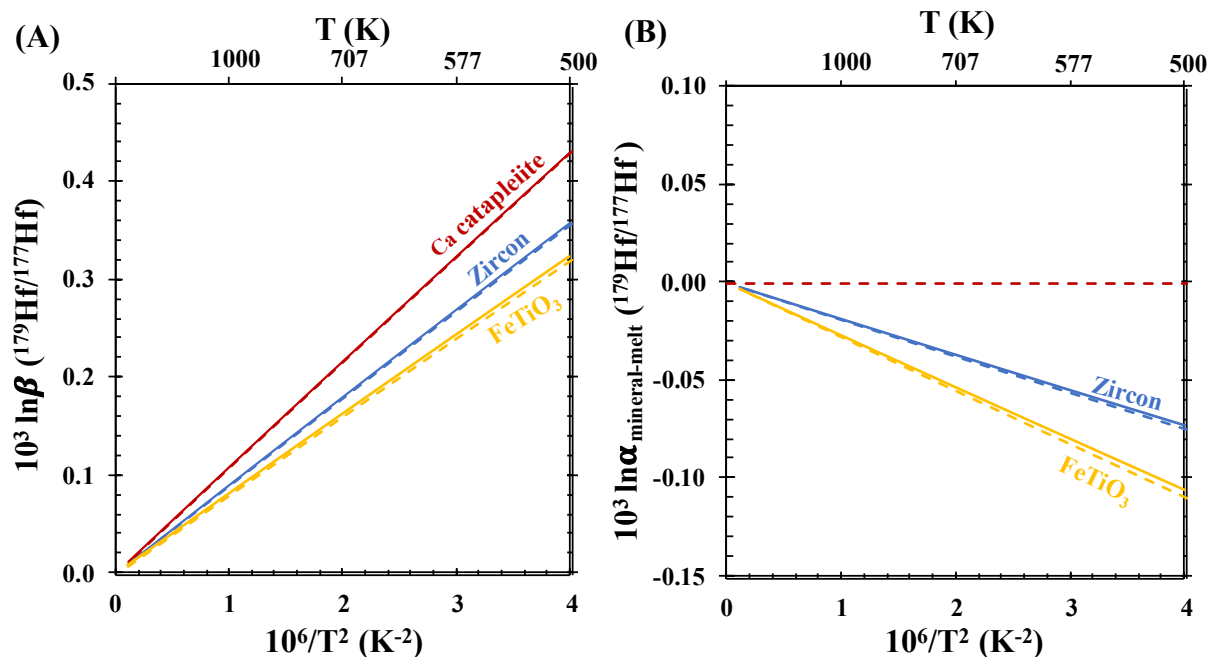
Figure 4. (A) Temperature-dependent 1000lnβ for Hf isotopes in zircon, ilmenite and Ca-catapleiite investigated in this study. (B) Temperature-dependent 1000lnα$_{mineral-melt}$ for Hf isotopes in zircon and ilmenite. As with Zr isotopes, the fractionation factors between minerals and melt are calculated by taking the difference between each mineral and Ca-catapleiite (which we use as silicate melt proxy). Solid and dash lines are calculation results for minerals with different Hf concentrations (see **Table 1** for details). Our results show that Hf stable isotope fractionation during equilibrium process is very limited.
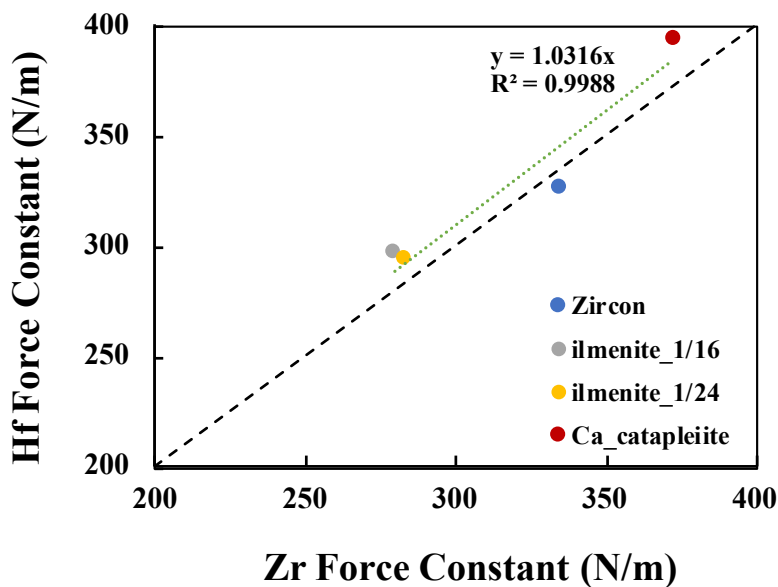
Figure 5. Zr and Hf mean force constants in several minerals (zircon, ilmenite with two concentrations, Ca-catapleiite). The current calculation results indicate that in minerals, Zr and Hf form bonds with nearly identical bond strengths. The black dashed line is the 1:1 line and the green dotted line is a regression through the data.
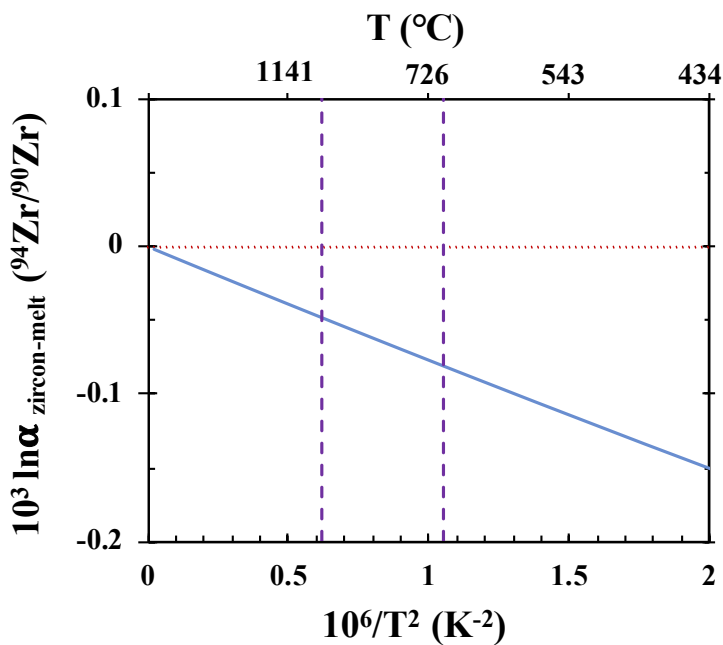
Figure 6. Zr isotope equilibrium fractionation factor between zircon and melt as a function of temperature. The two vertical dash lines bracket the temperatures relevant to igneous zircon crystallization of around 700-1000 °C.
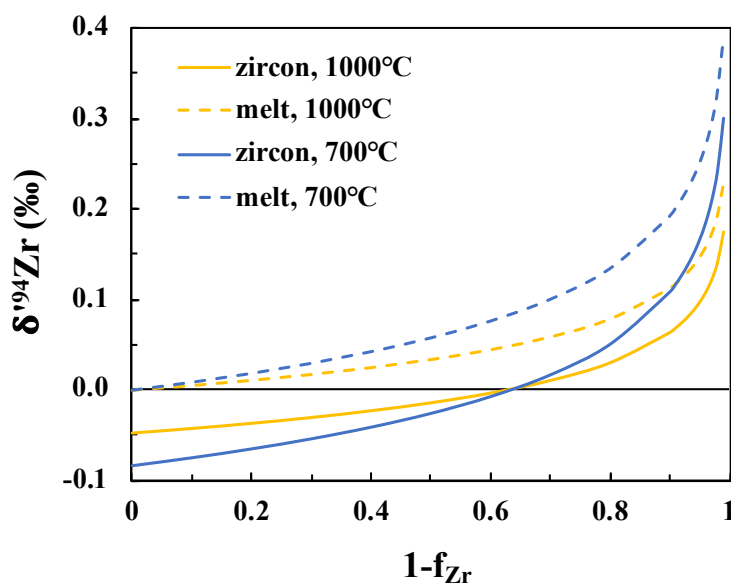
54

1374   **Figure 7**. δ'^{94}Zr in the instantaneous zircon and melt during Rayleigh distillation process at two
1375   temperatures of 700 and 1000 °C. f_{Zr} is the fraction of Zr remaining in the melt (see Eq. 18). $1 -$
1376 f_{Zr} is the fraction of Zr in zircon.
1377
1378

1379
1380
1381   **Figure 8.** Calculated trends of Zr/Hf and δ'^{94}Zr variations in instantaneous zircon assuming melt-
1382   zircon equilibrium at each step of a distillation. The free parameters are the fraction of Zr
1383   remaining in melt (f_{Zr} from 0.99 to 0.01) and the crystallization temperature. The calculations are
1384   done using equations 15 and 17, 21 and 22, with an initial Zr/Hf ratio of 31.1 and initial δ'^{94}Zr
1385   value of -0.086 ‰[66]. The zircon-melt equilibrium isotopic fractionation factor is $\Delta^{94}Zr^{eq}_{zircon\text{-}melt} =$
1386 $-\frac{7.87\times10^4}{T^2}$ (Sect. 4.1, Eq. 17). The red data point shows the current analytical uncertainties of
1387   Zr/Hf ratio ($\pm1\%$) and δ'^{94}Zr isotopic composition (±0.01‰). This figure can help test if zircon
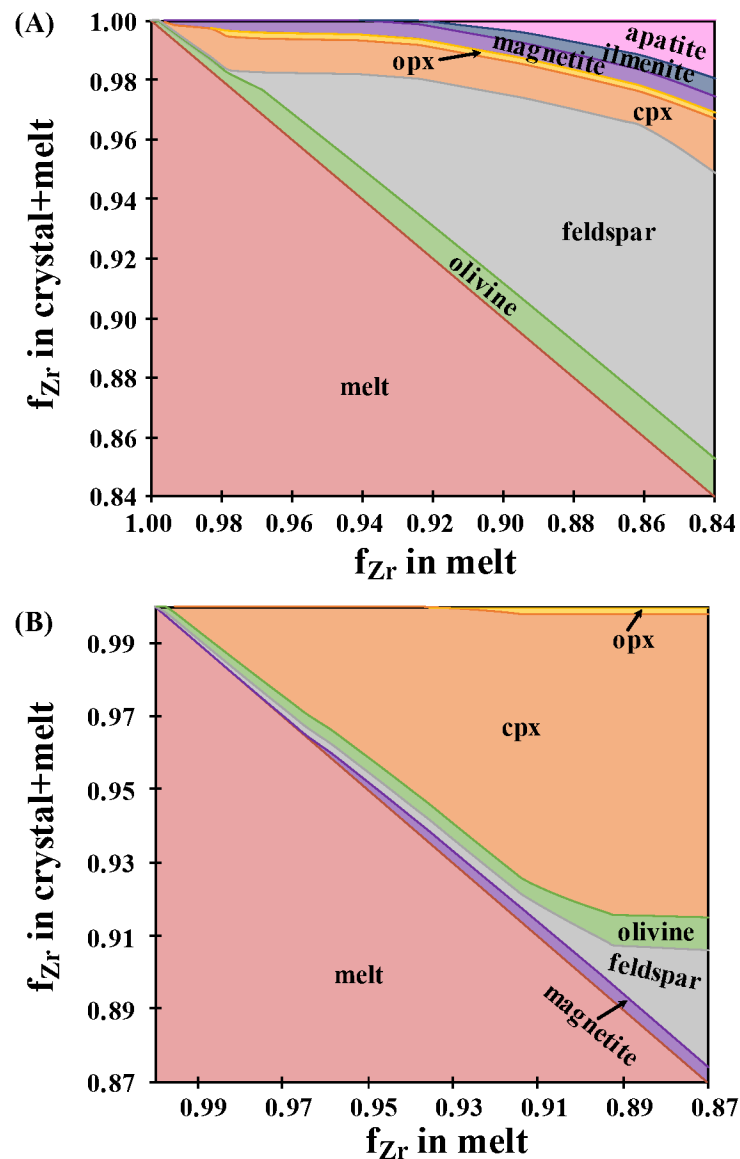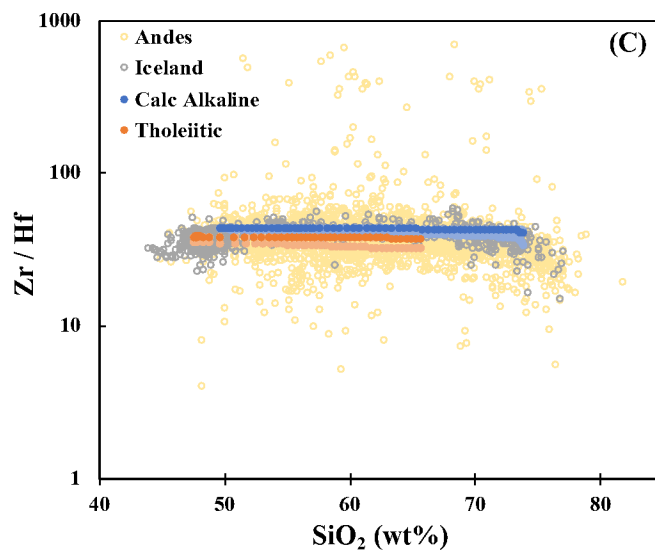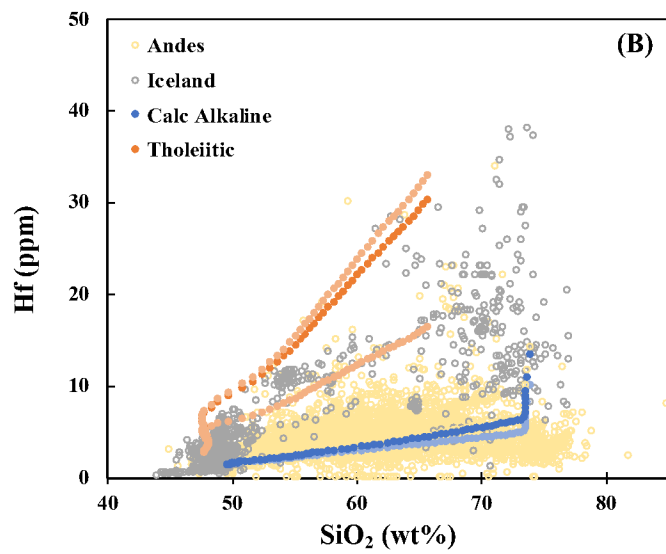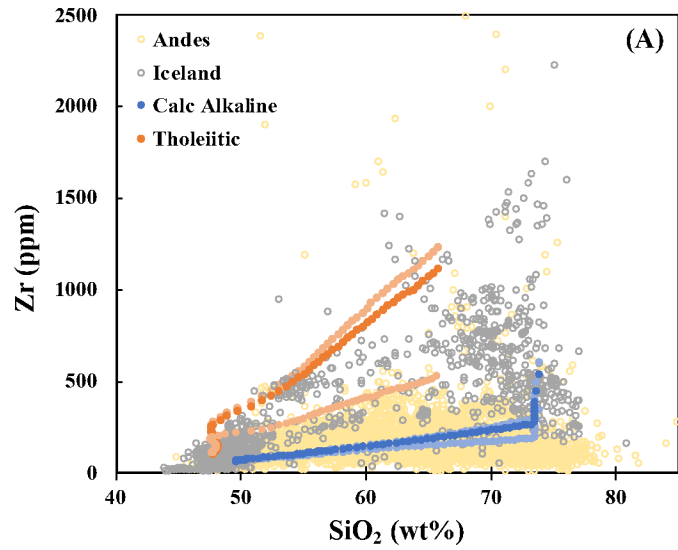1388   grew under equilibrium conditions.
1389
1390

Figure 9. Mass fractions of Zr in crystallized minerals and melt as a function of the mass fraction of Zr remaining in melt for (A) calc-alkaline and (B) tholeiitic magmas. Before zircon crystallization, only a small fraction of Zr is removed from the melt (mostly in clinopyroxene and feldspar), and here we use the geometric mean of the partition coefficients for each mineral. These calculations were run before zircon saturation (**Fig. S6**).

56

1
2
3
4
5
6
7
8
9
10
11
12
13
14
15
16
17
18
19
20
21
22
23
24
25
26
27
28
29
30
31
32
33
34
35
36
37
38
39
40
41
42
43
44
45
46
47
48
49
50
51
52
53
54
55
56
57
58
59
60

1400
1401

57

1402   **Figure 10.** (A) Zr and (B) Hf concentration and (C) Zr/Hf (weight ratio) evolutions during
1403   magmatic differentiation along calc-alkaline and tholeiitic series. Modeling was done using
1404   Rhyolite-MELTS and the results are compared with Andes (calc-alkaline) and Iceland (tholeiitic)
1405   rocks (compiled from the GEOROC database; see Sect. 4.2. for details). The darker color trends
1406   were calculated using the geometric mean of the partition coefficients compiled in GERM database,
1407   while the bracketing lighter color trends correspond to minimum and maximum partition
1408   coefficients.

1409

1410
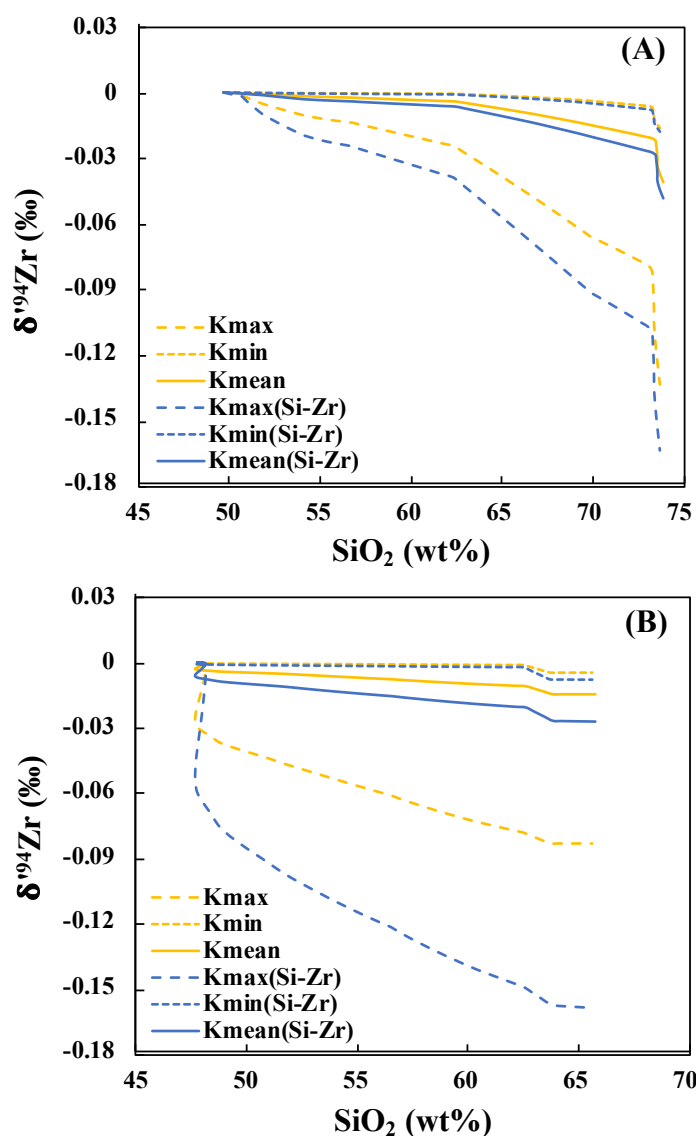
1411

1412

1413   **Figure 11.** Modelled evolution of the Zr isotopic composition of residual melt before zircon
1414   crystallization for (A) calc-alkaline and (B) tholeiitic magmas. The Zr isotopic fractionation factors
1415   between minerals and melt from our *ab initio* calculations were used in the modeling, using results
1416   from Rhyolite-MELTS as input (**Fig. 9**). The different trends are mainly caused by two factors: (i)
1417   the various bulk Zr partition coefficients used in our calculations and (ii) the different isotopic

58

1418 fractionation factors calculated using different substitution mechanisms for Zr in several silicate
1419 minerals. The blue lines labelled Si-Zr are calculated using $1000\ln\beta$ values for olivine, cpx and
1420 opx using the $^{IV}Si^{4+}\leftrightarrow Zr^{4+}$ substitution with minimum, mean, and maximum mineral/melt K values.
1421 The yellow lines are calculated using $1000\ln\beta$ values in olivine, cpx and opx using the $^{VI}Mg^{2+} +$
1422 $^{VI}Mg^{2+}\leftrightarrow Zr^{4+}+$ substitution with minimum, mean, and maximum mineral/melt K values. In all
1423 cases, the Zr isotopic compositions of the melts evolve towards lighter values before zircon starts
1424 to crystallize but the magnitude of this fractionation is relatively small given the current analytical
1425 precision on $\delta'^{94}Zr$ measurements ($\sim\pm0.01$ to ±0.04 ‰[66]).

1426
1427
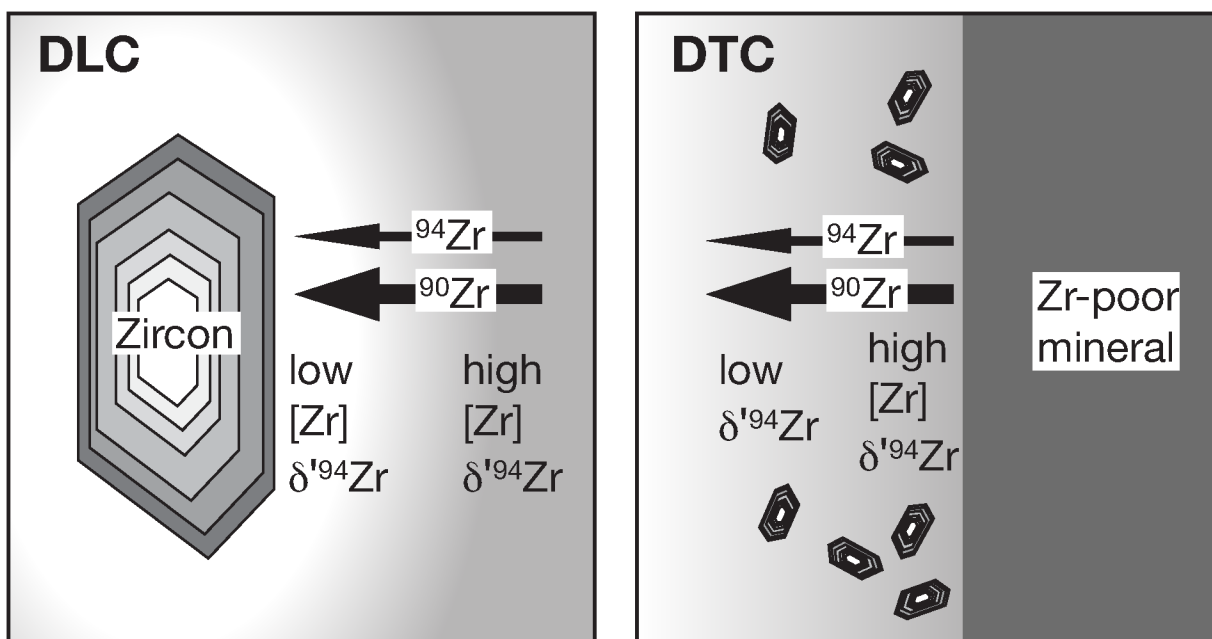
Figure 12. Schematic models of diffusive Zr isotopic fractionation during crystallization. **Left panel:** In the diffusion-limited crystallization model (DLC), the growth of zircon is limited by the diffusive supply of Zr to the surface from a far-field medium that is supersaturated. Because the light isotopes diffuse faster than the heavier ones, the liquid at the interface with the zircon will have low $\delta'^{94}Zr$, while further away from the interface the liquid will have high $\delta'^{94}Zr$. This model would predict zircons to have low $\delta'^{94}Zr$ but reservoir effects in the liquid would also lead to the crystallization of zircons with high $\delta'^{94}Zr$. **Right panel:** In the diffusion-triggered crystallization model (DTC), the growth of a Zr-poor mineral would push Zr away from the interface and lead to high $\delta'^{94}Zr$ at the interface in the liquid and low $\delta'^{94}Zr$ further away. The whole diffusive boundary layer would have elevated Zr concentration. This could trigger the saturation and crystallization of zircon, which would inherit some of the fractionated Zr isotopic composition from the diffusive boundary from which they grew.

1428
1429
1430
1431
1432
1433
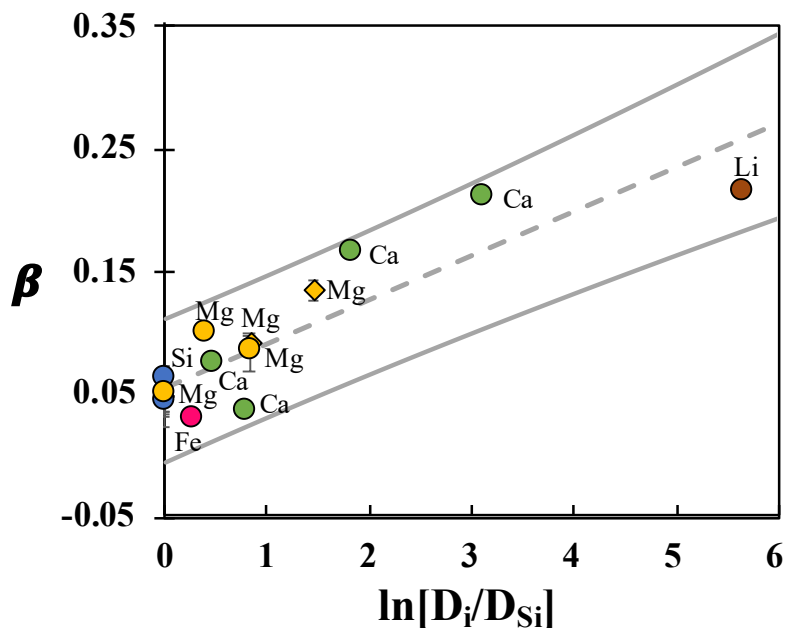1434
1435
1436
1437
1438
1439
1440
1441
1442
1443

Figure 13. β exponents as a function of the ratio of cation diffusivities normalized by those of Si in silicate melt (modified from Watkins et al.[140]). The β exponents for Zr and Hf isotopes were estimated by linearly regressing this trend to $\ln[D_{Zr}/D_{Si}]$ and $\ln[D_{Hf}/D_{Si}]$ ~0 because the diffusivities of both Zr and Hf are close to Si[141]. The two grey lines are the 95% prediction intervals. This empirical correlation correlates the degree of diffusion-driven isotopic fractionation (β) with a measure of solute-solvent interaction $\ln[D_i/D_{Si}]$[140]. In aluminosilicate melt, the solvent molecule is SiO_4^{4-}, which is the reason why the quantity $\ln[D_i/D_{Si}]$ is used to describe solute-solvent interaction.
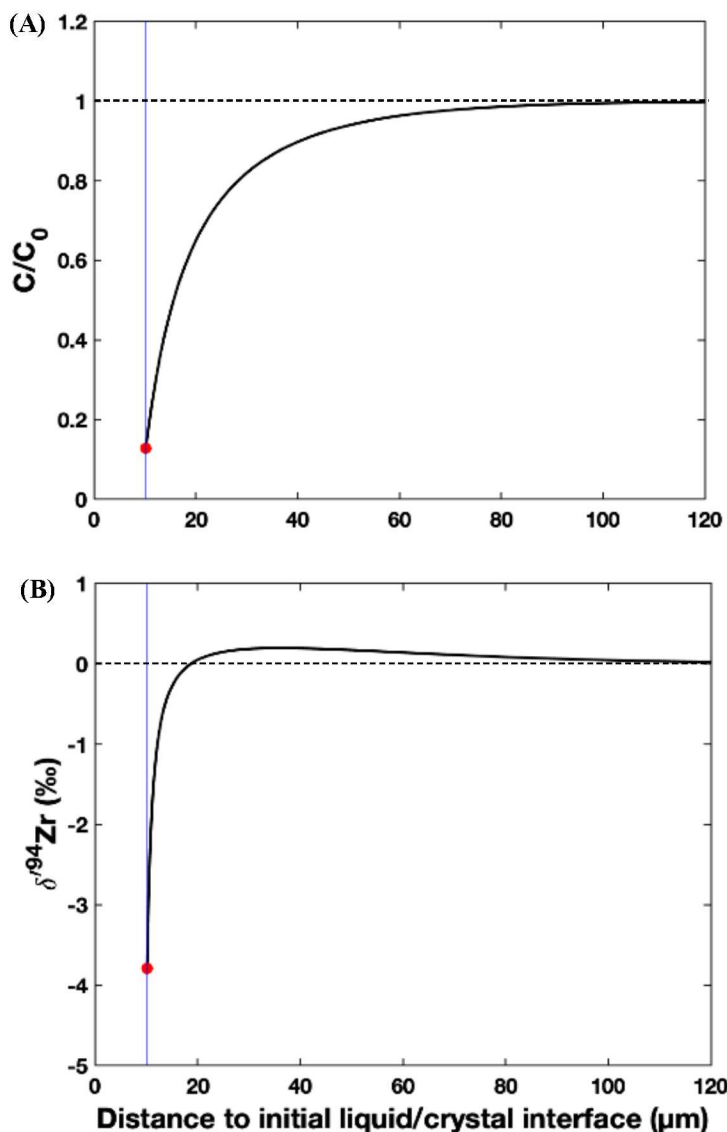
Figure 14. Zr concentration (A) and isotopic composition (B) profiles in the liquid away from the interface of a growing zircon in a diffusion-limited regime (DLC model) at the time when the zircon has reached 10 μm in size (the blue line is the liquid-solid interface). The red dot is the liquid concentration and isotopic composition at the interface. Both concentration and isotopic composition are relative to the liquid at infinity. As zircon grows from a supersaturated medium, the liquid and crystal near the liquid-crystal interface get enriched in the light isotopes of Zr due to their faster diffusion, while the liquid further away in the diffusive boundary layer gets enriched in the heavy isotopes due to their slower diffusion. The calculations were done using Eqs. 55, 49, 50 for diffusion-limited growth in a spherical geometry[133] with a Zr diffusivity of $D = 10^{-4}$ μm^2/s[142], Zr saturation concentrations $C_{sat} = 1806$ ppm[123], Zr concentration in zircon of 500,000 ppm, and a supersaturation $S = C_\infty/C_{sat} = 7.8$, a diffusive Zr isotopic fractionation factor $\Delta_D = -4.9$ ‰ ($\beta_{Zr} = 0.113$ in Eq. 24). (A and B correspond to **Movie 1 and 2**).
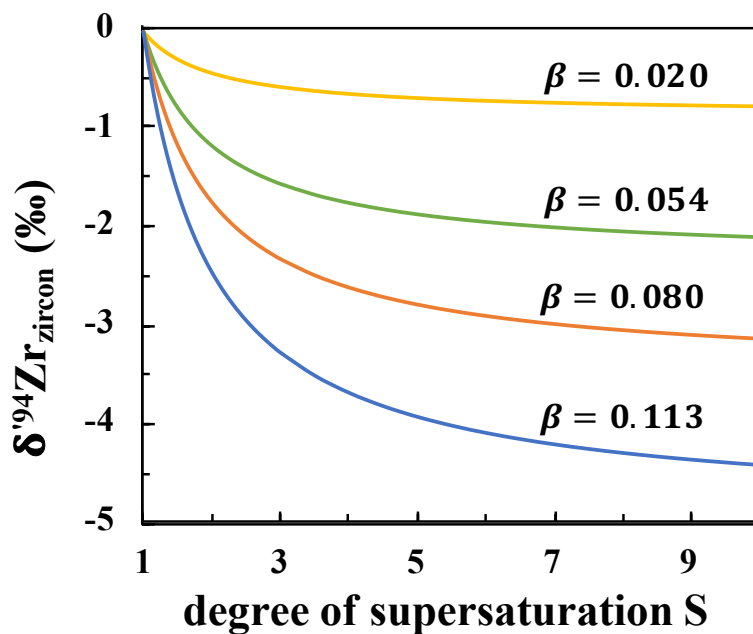
61

Figure 15. Expected δ'^{94}Zr variations in zircon as a function of the degree of supersaturation during diffusion-limited zircon growth from silicate melt with different diffusive β exponents for Zr isotopes (Eq. 26; see Sect. 4.3.1. for details). δ'^{94}Zr$_{zircon}$ is the isotopic composition in the crystal relative to that in the far-field growth medium.
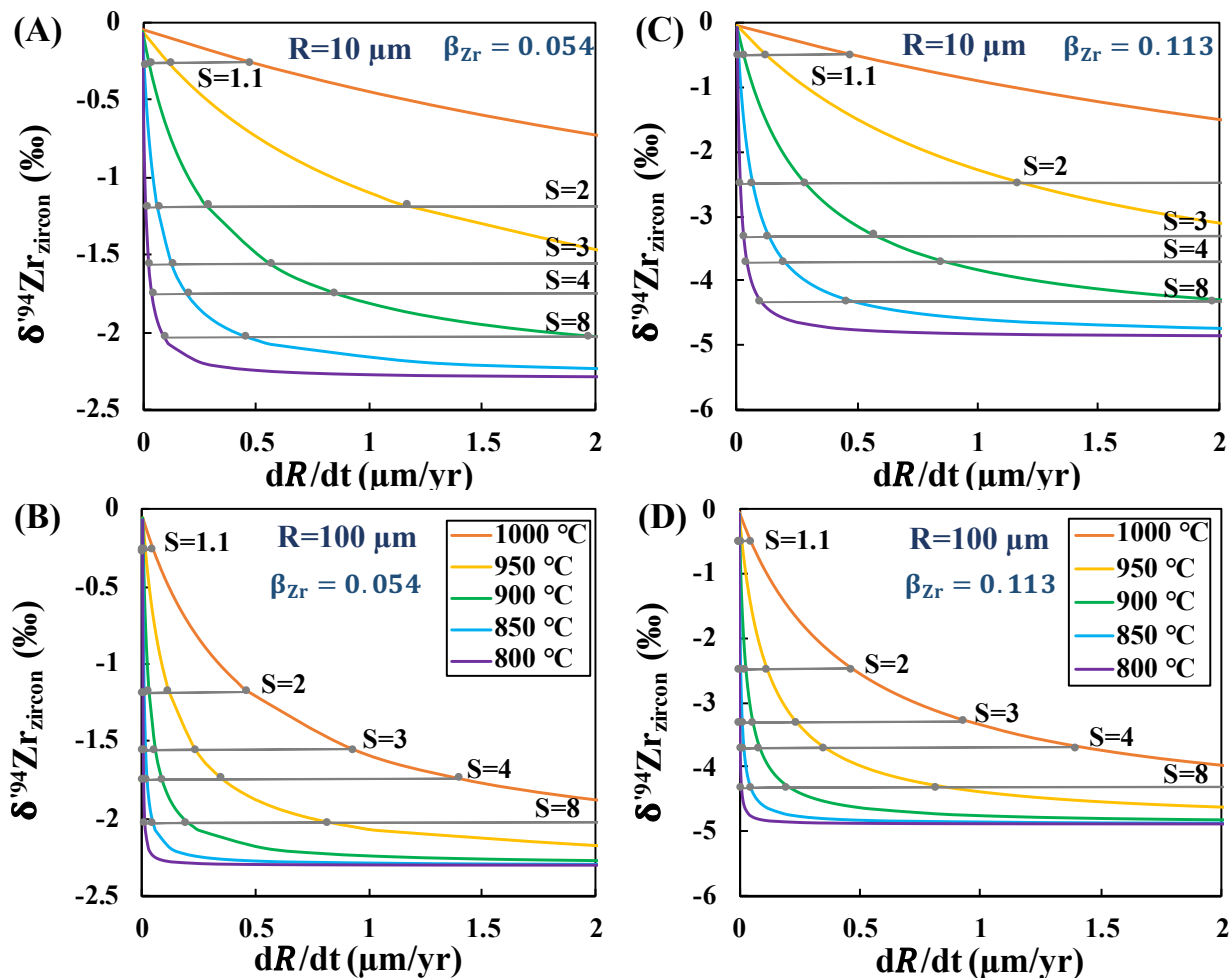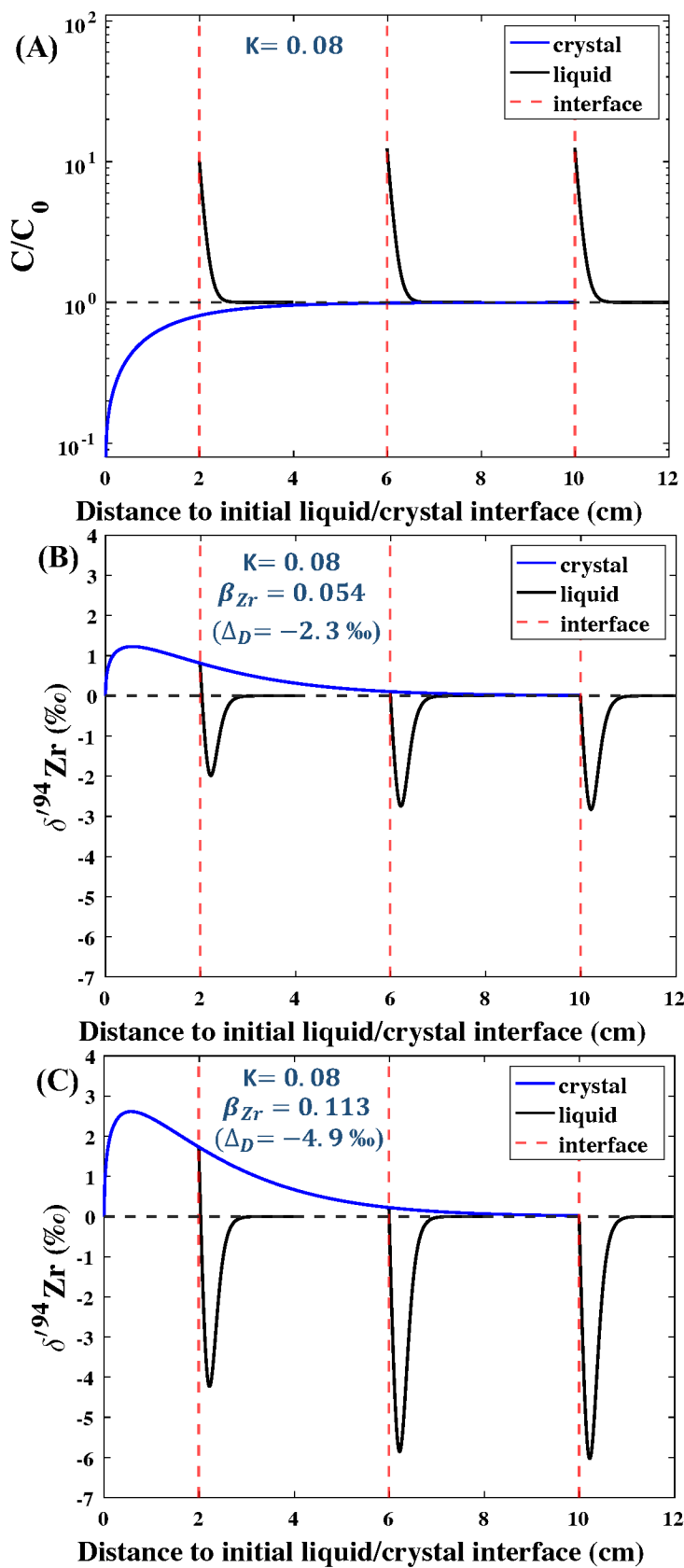
Figure 16. Expected $\delta'^{94}Zr$ fractionations in zircon as a function of growth rate at different temperatures and different supersaturations (Eqs. 26 and 30; see Sect. 4.3.1. for details). (A)-(B) use a diffusive Zr isotopic fractionation factor $\Delta_D = -2.3$ ‰ ($\beta_{Zr} = 0.054$ in Eq. 24); (C)-(D) use a diffusive Zr isotopic fractionation factor $\Delta_D = -4.9$ ‰ ($\beta_{Zr} = 0.113$ in Eq. 24). $\delta'^{94}Zr_{zircon}$ is the isotopic composition in the crystal relative to that in the far-field growth medium. This figure shows that measuring $\delta'^{94}Zr_{zircon}$ can help estimate the degree of supersaturation and zircon growth rate if the temperature can be independently constrained.
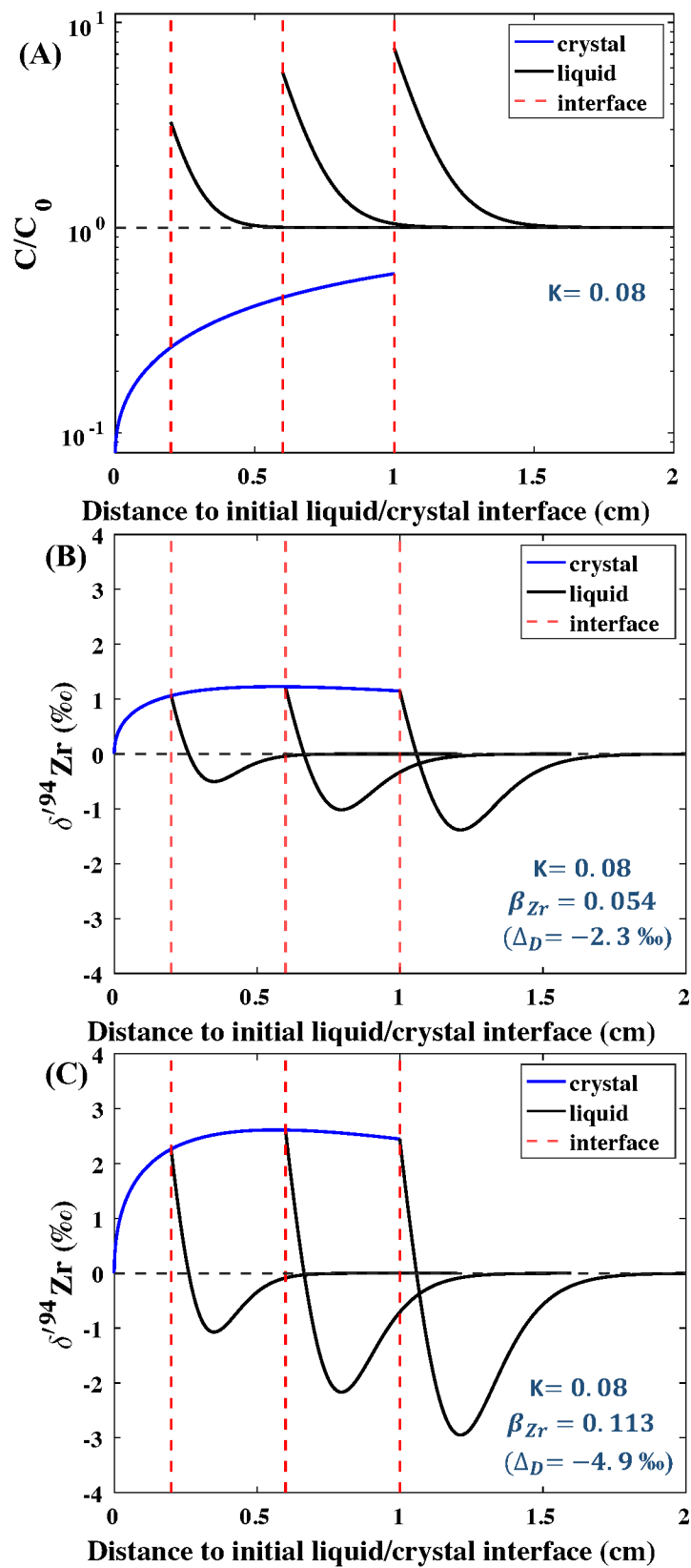
1
2
3   1493   **Figure 17**. Evolution of the Zr concentration (A) and isotopic composition (B, C) in a growing Zr-
4   1494   poor crystal (blue line) and in the surrounding melt growth medium (black line) in three snapshots
5   1495   taken at 0.6, 1.9, and 3.2 kyr (DTC model; see Sect. 4.3.2. for details). The concentration and
6   1496   isotopic composition are normalized to the far-field growth medium. The diffusive boundary layer
7   1497   has elevated Zr concentration, which could trigger zircon saturation and crystallization, thus
8   1498   inheriting the isotopic composition in the diffusive boundary layer. The curves were calculated
9   1499   using Eqs. 31-34, and A21, A23. We used the partition coefficient of clinopyroxene $K = 0.08$ (the
10   1500   geometric mean of the values compiled in GERM database), diffusivity for Zr in melt $D =$
11
12   1501 10^{-4} μm^2/s at 950 °C[142], a growth rate of $\dot{R} = 10^{-7}$ μm/s (so that $\dot{R}/D = 10$ cm^{-1} which is in
13   1502   the realm of possibilities[140]), and a diffusive isotopic fractionation factor $\Delta_D = -2.3$ and -4.9 ‰
14   1503   ($\beta_{Zr} = 0.054$ and 0.113 in Eq. 24, respectively). (A, B and C correspond to **Movie 3, 4 and 5**).
15
16   1504
17   1505
18
19
20
21
22
23
24
25
26
27
28
29
30
31
32
33
34
35
36
37
38
39
40
41
42
43
44
45
46
47
48
49
50
51
52
53
54
55
56
57   65
58
59

(A) K= 0.08

(B) K= 0.08
$\beta_{Zr} = 0.054$
$(\Delta_D = -2.3‰)$

(C) K= 0.08
$\beta_{Zr} = 0.113$
$(\Delta_D = -4.9‰)$

1506
1507

66

Figure 18. Same as **Fig. 17** but for a longer duration allowing the system to achieve steady-state (note that this calculation is not aimed at reproducing natural conditions as crystals would stop growing before reaching steady-state). Zr concentration (A) and isotopic composition (B, C) in the growing Zr-poor crystal (blue line) and in the melt growth medium (black line) in three snapshots taken at 6, 19, and 32 kyr. Note the difference in x-axis scale with **Fig. 17**. (A, B and C correspond to **Movie 6, 7 and 8**).
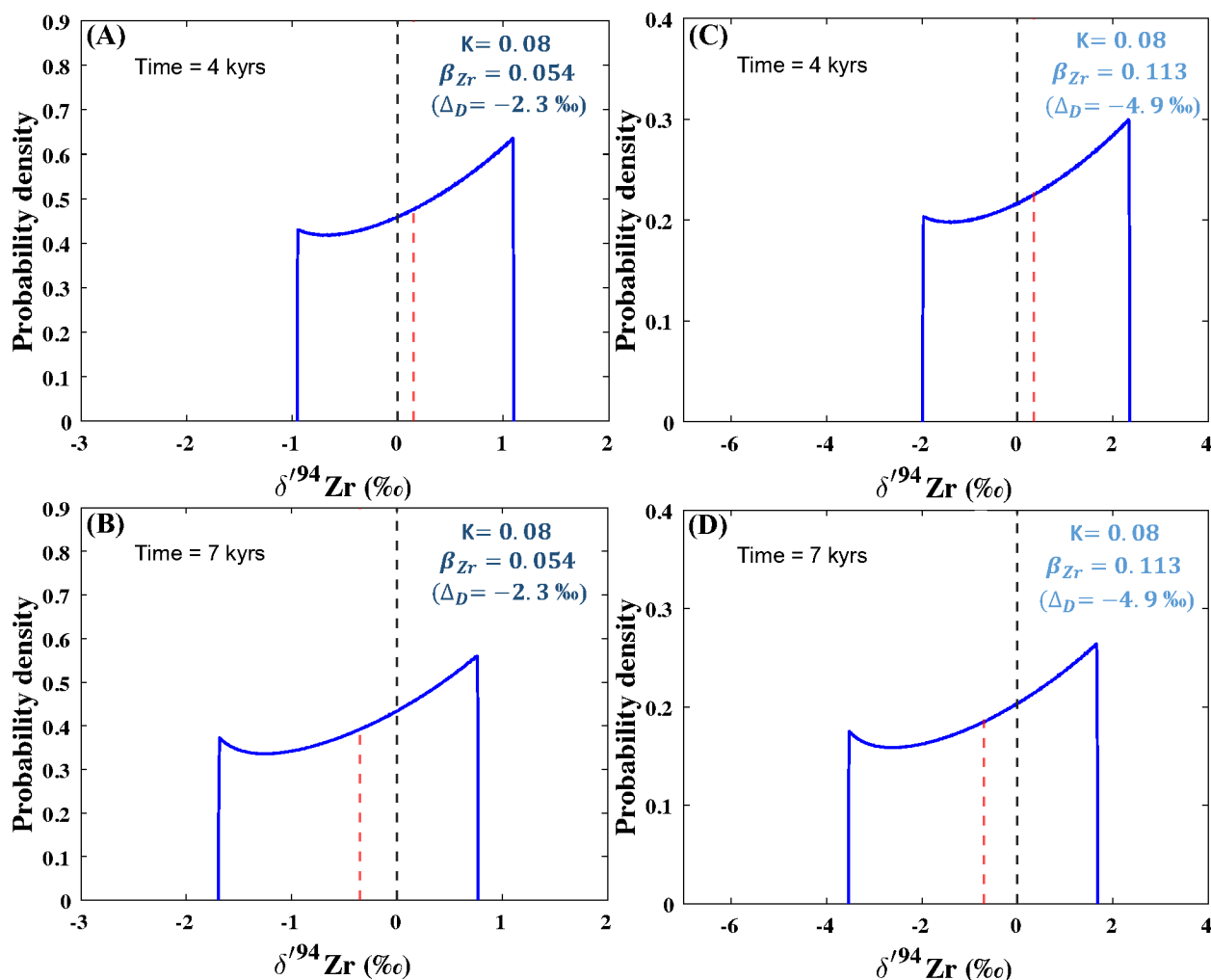
Figure 19. Expected probability density distribution functions (PDFs) of the Zr isotopic compositions of Zr atoms in the diffusive boundary layer around a low-Zr growing crystal at 4 and 7 kyr. The dashed red vertical line is the average isotopic composition of the boundary layer where the melt is Zr-supersaturated by at least of factor of 3. We only consider here locations where $C/C_0 > 3$ possibly conducive to zircon saturation. (A)-(B) use a diffusive Zr isotopic fractionation factor $\Delta_D = -2.3$ ‰ ($\beta_{Zr} = 0.054$ in Eq. 24); (C)-(D) use a diffusive Zr isotopic fractionation factor $\Delta_D = -4.9$ ‰ ($\beta_{Zr} = 0.113$ in Eq. 24). As the Zr-poor mineral grows (time increases from (A) to (B), or from (C) to (D)), the δ'^{94}Zr distributions of the diffusion-triggered crystallized (DTC) zircons shift to more negative δ'^{94}Zr values. (A, B and C, D correspond to **Movie 9 and 10**).

1527

Table 1. Average Zr-O and Hf-O bond lengths, coordination numbers (CN), force constant of Zr and Hf in relaxed mineral structures, and polynomial expansion coefficients of the reduced partition function ratios ($10^3 \ln\beta$) of $^{94}Zr/^{90}Zr$ and $^{179}Hf/^{177}Hf$ of the studied minerals.

clinopyroxene	Chemical composition	Average Zr-O bond length (Å)	CN	Zr Force constant (N/m)	Polynomial expansion coefficients[#]		
					A_1	A_2	A_3
$Si^{4+} \leftrightarrow Zr^{4+}$	$Mg_{24}Ca_{24}Si_{47}ZrO_{144}$ (2b, 3c)	1.985	4	524.3	1.09201	-5.903E-03	1.004E-04
	$Mg_{32}Ca_{32}Si_{63}ZrO_{192}$ (2a, 2b, 2c)	1.989	4	522.4	1.08785	-5.880E-03	1.000E-04
$*^{VI}Mg^{2+}+^{VIII}Ca^{2+} \leftrightarrow Zr^{4+}_{Mg}+$	$Mg_7ZrCa_7Si_{16}O_{48}$ (2c)	2.124	6	390.2	0.80773	-4.366E-03	7.472E-05
	$Mg_{15}ZrCa_{15}Si_{32}O_{96}$ (2b, 2c)	2.125	6	395.8	0.81756	-3.778E-03	4.405E-05
$*^{VI}Mg^{2+}+^{VI}Mg^{2+} \leftrightarrow Zr^{4+}_{Mg}+$	$Mg_6ZrCa_8Si_{16}O_{48}$ (2c)	2.117	6	371.5	0.77325	-5.224E-03	9.424E-05
orthopyroxene							
$Si^{4+} \leftrightarrow Zr^{4+}$	$Mg_{32}Si_{31}ZrO_{96}$ (2c)	1.976	4	538.2	1.12083	-6.059E-03	1.031E-04

68

	$Mg_{64}Si_{63}ZrO_{192}$ (2b, 2c)	1.975	4	540.0	1.12450	-6.078E-03	1.034E-04
$^{VI}Mg^{2+}$ (M1)+ $^{VI}Mg^{2+}$ (M2)	$Mg_{30}ZrSi_{32}O_{96}$ (2c)	2.131	6	409.0	0.85185	-4.604E-03	7.833E-05
$\leftrightarrow Zr^{4+}+$	$Mg_{62}ZrSi_{64}O_{192}$ (2b, 2c)	2.130	6	-			
olivine							
$Si^{4+}\leftrightarrow Zr^{4+}$	$Mg_{32}Si_{15}ZrO_{64}$ (2a, 2c)	1.970	4	562.3	1.17094	-6.329E-03	1.077E-04
	$Mg_{64}Si_{31}ZrO_{128}$ (2a, 2b, 2c)	1.969	4	566.4	1.17947	-6.376E-03	1.085E-04
$^{VI}Mg^{2+}$ (M2) + $^{VI}Mg^{2+}$ (M1)	$Mg_{30}ZrSi_{16}O_{64}$ (2a, 2c)	2.124	6	378.7	0.78861	-4.263E-03	7.252E-05
$\leftrightarrow Zr^{4+}+$	$Mg_{62}ZrSi_{32}O_{128}$ (2a, 2b, 2c)	2.123	6	380.1	0.79152	-4.278E-03	7.279E-05
quartz							
$Si^{4+}\leftrightarrow Zr^{4+}$	$Si_{80}ZrO_{162}$ (3a, 3b, 3c)	1.961	4	561.0	1.16823	-6.315E-03	1.074E-04
	$Si_{95}ZrO_{192}$ (4a, 4b, 2c)	1.960	4	-			
K-feldspar							
$^{IV}Al^{3+}+^{VIII}K^{+}\leftrightarrow Zr^{4+}_{Al}+$	$K_{7}Al_{7}Si_{24}O_{64}$ (2c)	1.969	4	540.1	1.12488	-8.154E-03	1.529E-04
	$K_{15}Al_{15}ZrSi_{48}O_{128}$ (2a, 2c)	1.968	4	544.3	1.13321	-8.215E-03	1.530E-04
apatite							

$^{IX}Ca^{2+} + {}^{VII}Ca^{2+} \leftrightarrow Zr^{4+} +$	$Ca_{38}ZrP_{24}O_{96}F_8$ (2a, 2b)	2.183	6	297.1	0.61798	-2.856E-03	3.330E-05
	$Ca_{78}ZrP_{48}O_{192}F_{16}$ (2a, 2b, 2c)	2.179	6	-			
geikielite							
$Ti^{4+} \leftrightarrow Zr^{4+}$	$Mg_{24}Ti_{23}ZrO_{72}$ (2a, 2b)	2.117	6	407.6	0.84873	-4.588E-03	7.805E-05
	$Mg_{48}Ti_{47}ZrO_{144}$ (2a, 2b, 2c)	2.116	6	410.0	0.85581	-4.626E-03	7.870E-05
ilmenite							
$Ti^{4+} \leftrightarrow Zr^{4+}$	$Fe_{24}Ti_{23}ZrO_{72}$ (2a, 2b)	2.129	6	279.6	0.58224	-3.147E-03	5.354E-05
	$Fe_{48}Ti_{47}ZrO_{144}$ (2a, 2b, 2c)	2.128	6	283.4	0.59015	-3.190E-03	5.427E-05
MgFe$_2$O$_4$ magnetite							
$^{VI}Fe^{3+} + {}^{IV}Fe^{3+} \leftrightarrow Zr^{4+}{}_{VI\text{-}Fe} + Mg^{2+}{}_{IV\text{-}Fe}$	$Mg_{17}ZrFe_{30}O_{64}$ (2a)	2.111	6	294.4	0.61306	-3.314E-03	5.638E-05
	$Mg_{33}ZrFe_{62}O_{128}$ (2a, 2b)	2.110	6	-			
tremolite							
$Si^{4+} \leftrightarrow Zr^{4+}$	$Mg_{40}Ca_{16}Si_{63}ZrH_{16}O_{192}$ (2a, 2c)	1.978	4	533.6	1.11117	-6.006E-03	1.0218E-04
$*^{VI}Mg^{2+}$ (M2) + $^{VI}Mg^{2+}$ (M1) $\leftrightarrow Zr^{4+}{}_{M2} +$	$Mg_{18}ZrCa_8Si_{32}H_8O_{96}$ (2c)	2.113	6	383.3	0.79930	-4.320E-03	7.350E-05

70

	Chemical composition	Average Hf-O bond length (Å)	CN	Hf Force constant (N/m)	A_1	A_2	A_3
	$Mg_{38}ZrCa_{16}Si_{64}H_{16}O_{192}$ (2a, 2c)	2.112	6	-			
pyrope							
$^{IV}Si^{4+} \leftrightarrow Zr^{4+}$	$Mg_{24}Al_{16}Si_{23}ZrO_{96}$	1.979	4	512.7	1.06679	-9.705E-03	1.902E-04
$*^{VI}Al^{3+} + {}^{IV}Si^{4+} \leftrightarrow Zr^{4+} + Al^{3+}$	$Mg_{24}Al_{16}Si_{23}ZrO_{96}$	2.074	6	433.5	0.90215	-7.151E-03	1.354E-04
$^{VIII}Mg^{2+} + {}^{VIII}Mg^{2+} \leftrightarrow Zr^{4+} +$	$Mg_{22}ZrAl_{16}Si_{24}O_{96}$	2.240	8	345.7	0.71955	-4.862E-03	8.769E-05
zircon	$Zr_2Si_2O_8$	2.228	8	334.7	0.69698	-3.767E-03	6.409E-05
baddeleyite	Zr_4O_8	2.187	7	323.4	0.67268	-3.109E-03	3.624E-05
Ca-catapleiite	$Ca_4Zr_4Si_{12}H_{16}O_{44}$	2.114	6	369.2	0.77571	-5.704E-03	1.226E-04

	Chemical composition	Average Hf-O bond length (Å)	CN	Hf Force constant (N/m)	Polynomial expansion coefficients#		
					A_1	A_2	A_3
zircon	$**Zr_{15}HfSi_{16}O_{64}$ (2a, 2b, 2c)	2.140	8	327.3	0.09094	-4.01E-04	7.49E-06
	$Zr_{31}HfSi_{32}O_{128}$ (2a, 2b, 2c)	2.140	8	326.4	0.09067	-4.00E-04	7.46E-06
ilmenite	$**Fe_{16}Ti_{15}HfO_{48}$ (2a, 2b, 2c)	2.092	6	297.1	0.08254	-3.64E-04	6.79E-06
	$Fe_{24}Ti_{23}HfO_{72}$ (2a, 2b)	2.092	6	294	0.08167	-3.60E-04	6.72E-06

71

Ca-catapleiite	$Ca_4Zr_3HfSi_{12}H_{16}O_{44}$	2.081	6	393.3	0.10928	-4.82E-04	8.99E-06
	$Ca_8Zr_7HfSi_{24}H_{32}O_{88}$ (2a)	2.082	6	394.1	0.10951	-4.83E-04	9.01E-06

1531

1532   represents vacancy.

1533   #The polynomial expansion equation is: $10^3ln\beta=A_1 x+A_2 x^2+A_3 x^3$, where $x=10^6/T^2$. T is temperature in Kelvin.

1534   Abbreviations after chemical formulas refer to the expansion way of primitive cells to generate supercells and investigate the effect of

1535   dilution. For instance, "2a, 2b, 2c" represents the supercell is generated by expanding the primitive cell twice along a, b, and c directions.

1536   *These substitutions are favored by spectroscopic observations[103].

1537   **The primitive cells of zircon ($Zr_2Si_2O_8$) and ilmenite ($Fe_2Ti_2O_6$) are used to construct the supercell.

1538

1539

72

1540
1541 **For TOC Only**
1542
1543

1544
1545